AAPS PharmSciTech (2025) 26:81
https://doi.org/10.1208/s12249-025-03069-9

RESEARCH ARTICLE

Nanoparticle Formulations for Intracellular Delivery in Colorectal Cancer Therapy

Burcu Uner[1] · Erdogan Oguzhan Akyildiz[2,3] · Kubra Kolci[4,5] · Rengin Reis[4]

Received: 11 October 2024 / Accepted: 10 February 2025 / Published online: 7 March 2025

Abstract

This study introduces advanced nanoparticle-based drug delivery systems (NDDS) designed for targeted colorectal cancer treatment. We developed and characterized three distinct formulations: Bevacizumab-loaded chitosan nanoparticles (BEV-CHI-NP), polymeric micelles (BEV-PM), and BEV-conjugated exosomes enriched with AS1411 and N1-methyladenosine (AP-BEV + M1A-EXO). Each formulation exhibited optimized physicochemical properties, with particle sizes between 150 and 250 nm and surface charges ranging from + 14.4 to + 43 mV, ensuring stability and targeted delivery. The AP-BEV + M1A-EXO formulation demonstrated targeted delivery to VEGF, a protein commonly overexpressed in colorectal cancer cells, as indicated by localized staining. This suggests a more precise delivery of the therapeutic agent to VEGF-enriched regions. In contrast, the BEV-CHI-NP formulation exhibited a broader pattern of tumor suppression, evidenced by reduced overall staining intensity. The BEV-PM group showed moderate effects, with a relatively uniform protein expression across tumor tissues. *In vivo* studies indicated that the AP-BEV + M1A-EXO formulation achieved a notable reduction in tumor volume (~ 65.4%) and decreased levels of tumor biomarkers, including CEA and CA 19–9, compared to conventional BEV-API treatment. *In vitro* experiments using human colon tumor organoids (HCTOs) further supported these findings, showing a significant reduction in cell viability following exposure to AP-BEV + M1A-EXO. These results suggest that combining aptamer specificity with exosome-based delivery systems could enhance the precision and effectiveness of colorectal cancer therapies, representing a potential advancement in treatment strategies. *In vivo* experiments further revealed that the AP-BEV + M1A-EXO formulation outperformed conventional BEV-API treatment, achieving a four-fold increase in tumor suppression. This formulation resulted in a 65.4% reduction in tumor volume and a significant decrease in tumor biomarkers, including CEA and CA 19–9. *In vitro* studies also demonstrated a significant reduction in cell viability in human colon tumor organoids exposed to AP-BEV + M1A-EXO. These findings highlight the potential of combining aptamer specificity with exosome-based delivery systems to enhance the precision and efficacy of colorectal cancer therapies, marking a promising step forward in cancer treatment innovation.

New concept statement The manuscript presents a novel concept of dual nucleus and mitochondria targeting for colorectal cancer therapy through exosome and nanoparticle-based delivery systems. This innovative approach combines the specificity of the AS1411 aptamer with modified nucleosides like N1-methyladenosine, conjugated to exosomes for enhanced delivery of Bevacizumab. What sets this approach apart from existing research is its dual-targeting mechanism, where Bevacizumab disrupts extracellular angiogenesis, while the aptamers modulate intracellular processes like tRNA and mtRNA regulation. This synergistic strategy significantly improves therapeutic outcomes by increasing tumor suppression and reducing cancer biomarkers. The insights gained contribute to materials science by demonstrating the potential of exosome-based systems to improve the precision, stability, and multi-target functionality of cancer therapies, representing a significant advancement in nanoparticle-based drug delivery systems for solid tumors.

Extended author information available on the last page of the article

Keywords AS1411 aptamer · colorectal cancer · exosome therapy · M1A · nanoparticle-based drug delivery systems · organoid · targeted delivery

Introduction

Colon cancer remains a major public health challenge worldwide, accounting for a significant proportion of cancer-related morbidity and mortality [1, 2]. Despite advancements in surgical techniques and chemotherapy regimens, the survival rates for advanced-stage colon cancer remain dismal. The urgent need for more effective and targeted therapies has driven extensive research into innovative drug delivery systems that can enhance the precision and efficacy of treatment, while minimizing off-target effects [3–6].

One of the most promising strategies in the field of targeted therapy for colon cancer involves the use of novel drug delivery systems (NDDS). Nanoparticles can be engineered to improve the pharmacokinetics and biodistribution of therapeutic agents, allowing for their selective accumulation in tumor tissues [7–9]. This selective delivery is often achieved by exploiting the enhanced permeability and retention (EPR) effect, which is characteristic of tumor vasculature. However, the specificity and efficiency of these delivery systems can be further enhanced by functionalizing the nanoparticles with ligands or aptamers that specifically recognize and bind to receptors overexpressed on cancer cells.

Bevacizumab (BEV), a monoclonal antibody that targets vascular endothelial growth factor (VEGF), has been widely used in the treatment of various cancers, including colon cancer [10–12]. By inhibiting VEGF, BEV effectively reduces angiogenesis, a critical process for tumor growth and metastasis. However, the therapeutic potential of BEV is often limited by its poor penetration into solid tumors and its short half-life in circulation. To address these limitations, BEV has been incorporated into various nanoparticle formulations, which can improve its stability, prolong its circulation time, and enhance its accumulation in tumor tissues [12, 13].

The use of aptamers, such as AS1411, represents another innovative approach to enhancing the specificity of drug delivery systems. AS1411 is a G-quadruplex DNA aptamer that selectively binds to nucleolin, a protein that is overexpressed on the surface of cancer cells, including colon cancer cells [14, 15]. Nucleolin is involved in various cellular processes, including ribosome biogenesis, DNA repair, and apoptosis regulation. By targeting nucleolin, AS1411 can facilitate the selective delivery of therapeutic agents to cancer cells, thereby increasing the efficacy of the treatment while reducing systemic toxicity. Recent studies have demonstrated that AS1411-conjugated nanoparticles can significantly enhance the therapeutic efficacy of various anticancer agents, including those targeting colon cancer [15].

N1-methyladenosine (M1A) is a modified nucleoside that has recently gained attention as a potential biomarker and therapeutic target in cancer. M1A is involved in the regulation of mRNA translation and stability, and its dysregulation has been implicated in the development and progression of various cancers, including colon cancer [16, 17]. The incorporation of M1A into nanoparticle-based drug delivery systems has been shown to enhance the targeting and efficacy of anticancer therapies. Specifically, M1A-modified nanoparticles can selectively bind to and modulate the activity of specific RNA molecules in cancer cells, leading to the inhibition of tumor growth and induction of apoptosis [18]. In the present study, we aimed to develop and characterize a novel nanoparticle-based drug delivery system for the targeted treatment of colon cancer. Our formulation incorporated Bevacizumab into chitosan-based nanoparticles (BEV-CHI-NP) and micelles (BEV-PM), as well as AS1411 and M1A loaded exosomes (AP-BEV + M1A-EXO). The formulations were designed based on experimental design principles and subjected to extensive characterization, including transmission electron microscopy (TEM), dynamic light scattering (DLS), and high-performance liquid chromatography (HPLC) analysis. In addition, in silico release and docking studies were conducted to predict the release profiles and interactions of the formulations with their target molecules.

To evaluate the therapeutic potential of these formulations, we conducted *in vitro* release studies, followed by *in vivo* experiments using a colon cancer animal model. Carcinoembryonic antigen (CEA), Thymidylate synthase (TYMS), carbohydrate antigen 19–9 (CA19-9), and carbohydrate antigen 125 (CA125) levels were also investigated before and after treatment to assess the impact of the formulations on tumor markers. Western blot, ELISA, and PCR analyses were performed on tissue and blood samples collected from the animal study to assess the expression levels of key molecular markers associated with the apoptotic pathway. Our results demonstrated that the AS1411 and M1A components significantly enhanced the therapeutic efficacy of the formulations, leading to increased apoptosis, inhibition of tumor growth, and significant reductions in CEA, TYMS, CA19-9, and CA125 levels (Fig. 1).

Material and Methods

Materials

Formulation Preparation and Solvents

Bevacizumab (BEV)(#A2006) was purchased from Selleckchem (Houston, TX, USA). Poly(ε-caprolactone)$_{1000}$-b-PEG$_{2000}$

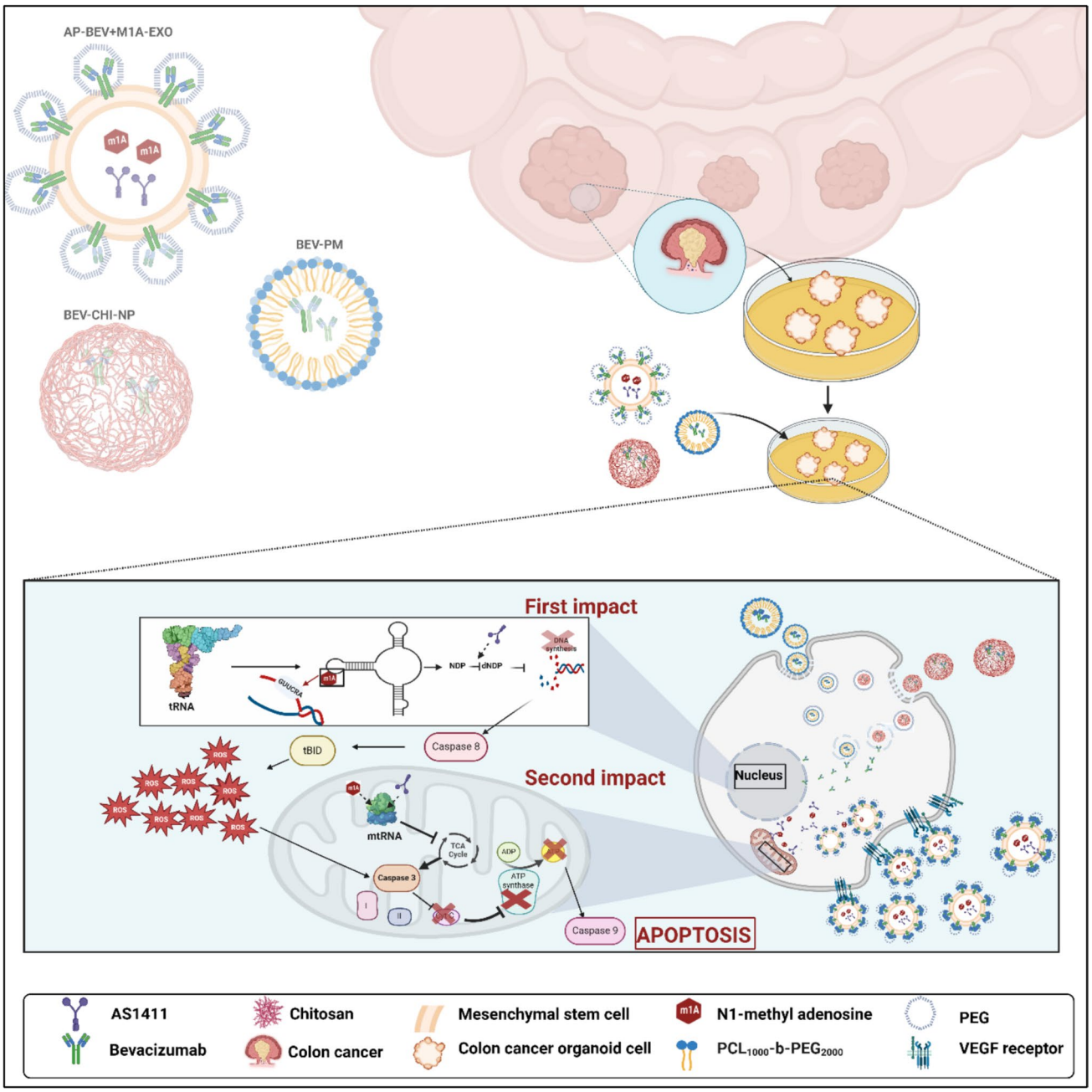

Fig. 1 Targeted delivery of bevacizumab-conjugated exosomes, bevacizumab loaded micelles and chitosan nanoparticles for inducing apoptosis in colon cancer cells (Created with BioRender.com)

diblock polymer ($PCL_{1000}PEG_{2000}$)(#900,670), chitosan (CHI)(#419,419), 1-methyladenosine (colon cancer derived) (M1A)(#SMB00939), pyrene (#129–00-00), Reinecke salt (#183,687), Simplicon® Human iPS Cell Line (#SCC271), RNA Reprogramming Kit (#SCR550), Accumax™ (#A7089), SILu™MAb BEV—stable isotope labeled (SIL) monoclonal antibody (mAb) standard (#MSQC21), ECM Gel (#CC131), CdSe/ZnS core–shell type quantum dots (#919,144), and human ES/iPS Leibovitz's L-15 medium (#SCM130) were obtained from Sigma (St. Louis, MO, USA). Anti-Nucleolin Aptamer (AS1411) (#A321259) was sourced from Antibodies.com (Cambridge, UK). Whilst the exosome-human CD9 isolation reagent (#10614D) was acquired from Thermo Fisher (Waltham, MA, USA), all solvents that using preparation and analysis phase were HPLC grade.

Biological Markers

cDNA kit and master mix (#11,756,500), RNeasy kit (#73,404), Trizol agent (#10,296,028), Hematoxylin solution modified acc. to Gill III (#1.05174), human carbohydrate antigen (Ag) CEA ELISA Kit (#RAB0375), human carbohydrate Antigen 125 / Mucin-16 ELISA Kit (#RAB0376), human carbohydrate Antigen 19–9 ELISA Kit (#RAB0373), Anti-CEA (CD66e) antibody (ab), rabbit monoclonal (#SAB5600137), anti-TYMS ab produced in rabbit (#SAB5700001), anti-carbonic anhydrase 9 (CA19-9) ab produced in rabbit (#SAB5701575), and anti-CA125 / MUC16 ab, and clone 4Z2L4, Rabbit Monoclonal (#SAB5702541) ab were acquired from Sigma Aldrich (St. Louis, MO). Mount-Quick Mounting Media (#04980-AB), Eosin (#Z02568), Hematoxylin (#04980-AB), Xylene I (#Z02595), and Xylene II(#Z02591) were purcha sourced from Structure Probe (West Chester, PA, USA).

Organoids and Cell Culture

Normocin (#ant-nr-1), and Primocin (#ant-pm-1) were purchased from Invivogen (San Diego, CA, USA). Gentamicin (#E737) was procured from Amresco (Framingham, MA, USA). 1X Pen/Strep (#15,070,063), HEPES (#15,630,080), and TryplE Express (#12,604,039) were sourced from ThermoFisher (Waltham, MA, USA). DMEM (#12,634,028), 1X Glutamax (#35,050,061), 1X B27 (#12,587,010), and 1X N2 (#17,502,048) were all sourced from Life Technologies (Carlsbad, CA, USA). L-WRN cell line (CRL-3276) and Dulbecco's Phosphate Buffered saline (D-PBS, 1X, #30–2200 ™) were procured from ATCC (Manassas, VA, USA). Nicotinamide (#N0636), N-acetyl cysteine (#A9165), SB202190 (#S7067), Gastrin I (# G9020), and A83-01 (#SML0788) were all acquired from Sigma Aldrich (St. Louis, MO, USA) CellTiter-Glo 3D (#G9681) was procured from Promega (Madison, WI, USA).

Y-27632 (Cat# 1254) was purchased from Tocris (Bristol, UK). Lastly, while EGF (#AF-100–15,) was supplied from Peprotech (Cranbury, NJ, USA), Matrigel using Cell Recovery Solution (CRS) (# 354,253) was obtained from Corning (Corning, NY, USA).

Formulation Design

To optimize the three different nano delivery systems developed for this study, we employed Response Surface Methodology (RSM) using a Central Composite Design (CCD). Key formulation variables were identified, including the concentration of BEV, the ratio of $PCL_{1000}PEG_{2000}$ to chitosan, and the amounts of M1A and AS1411. These factors were selected based on their critical roles in determining the characteristics of the nanoparticles and exosomes; particle size, drug encapsulation efficiency (%EE), and release kinetics. A series of experiments were conducted according to the CCD matrix, systematically varying the levels of these factors to evaluate their effects on the response variables. The data collected were then used to build a quadratic model, which allowed for the prediction of optimal formulation conditions (Supplementary File-S1). The model's predictions were validated through additional experiments, confirming the reliability of the optimized parameters.

Preparation of NDDS

BEV-PM

Before preparation of the BEV-PM, critical micelle concentration (CMC) of the $PCL_{1000}PEG_{2000}$ micelles was measured using pyrene as a fluorescent probe to detect appropriate amount of polymer to make stabile micelle formulation [19]. A series of aqueous solutions of the copolymer, with concentrations ranging from 5×10^{-5} to 0.5 mg/mL, was prepared. A known amount of pyrene was added to each solution, resulting in a final pyrene concentration of 6.2×10^{-6} M. These solutions were incubated at 36°C in the dark with gentle agitation for 20 h. The samples were then excited at 334 nm using an Agilent 8453 G1103A Spectrophotometer (Santa Clara, CA, USA). All measurements were performed at room temperature. The ratio of the first to the third intensity peaks was plotted against the logarithm of the copolymer concentration to determine the CMC.

$PCL_{1000}PEG_{2000}$ was combined with BEV (2.5 mg/ml) in distilled water at 37°C to prepare BEV-NP. The resulting micelles were purified through dialysis using a Pro 6 Membrane with a molecular weight cut-off (MWCO) of 8,000 (Fisher Scientific, Waltham, MA, USA), followed by ultrafiltration with a MWCO of 40,000 to obtain the BEV-NP. The BEV content within the micelles was quantified using inductively coupled plasma mass spectrometry, conducted on a Waters Alliance Radio Mass Spectroscopy system (Milford, MA, USA) equipped with a Waters™ SQ Detector 2.

BEV-CHI-NP

To protect BEV from the detrimental effects of acid exposure, PEG was employed as a protective agent [20]. The process began by dissolving PEG at a concentration of 2.5% w/w in an acidic solution composed of 2% acetic acid, which also contained 4% w/w CHI. Once the PEG was fully

dissolved, BEV was introduced into the CHI-PEG mixture at a concentration of 2.5 mg/mL. The addition of BEV was carried out under conditions that minimized light exposure to prevent any potential degradation. The entire mixture was then subjected to stirring at a constant speed of 400 rpm for 1 h, ensuring thorough mixing and proper interaction between the components.

AP-BEV + M1A-EXO

Isolation of the Exosomes

iPSCs were cultured in Leibovitz's L-15 medium supplemented with 15% exosome-depleted FBS. The natural exosomes in the FBS were removed by overnight ultracentrifugation at 4000 rpm at 4°C, followed by filtration through a 0.22 µm filter (Millipore, USA). After 48 h of culture, the medium supernatant was collected. Cells and cellular debris were initially removed by centrifugation at 1500 rpm for 15 min at 4°C, followed by a second centrifugation at the same speed for another 15 min. Large vesicles were eliminated by ultracentrifugation and subsequent filtration through a 0.22 µm filter. Exosomes were then isolated by ultracentrifugation at 4000 rpm for 3 h at 4°C. The exosome pellet was resuspended in PBS, and the concentration of exosomes derived from iPSCs was measured using differantial light scattering (DLS).

Conjugation with BEV and PEGylation

BEV-conjugated exosome (100 µL at 2.5 µg/µL) were incubated with CD9 Isolation Reagent (10 µL) in PBS buffer at 37°C for 30 min. To eliminate any unbound probes, the exosome were washed twice with PBS by ultracentrifugation at 4000 RPM for 90 min at 4°C [21]. The resulting pellet was resuspended in PEGylated (1.5%, w/w) PBS buffer. The presence of BEV on the surface of the exosome was then assessed using Agilent 8453 G1103A Spectrophotometer (λex = 588 nm, λem = 604 nm) (Supplementary File-S2).

The binding kinetics of BEV to exosome was evaluated using surface plasmon resonance (SPR) with a WAVE Delta Grating-Coupled Interferometry (GCI) system (Malvern Panalytical, Waltham, MA, USA). Measurements were conducted with HBS buffer (20 mM HEPES, 250 mM NaCl, 3.5 mM EDTA, 0.005% polysorbate 20, pH 7.4) as the running buffer, while ligand immobilization was performed using HBS buffer supplemented with 700 mM NaCl. For ligand immobilization, a GCI sensor chip (Malvern) was activated by flowing a solution of 20 mM EDAC and 5 mM Sulfo-NHS (Malvern) across the surface for 420 s at a rate of 30 µL/min. BEV was immobilized at a concentration of 2.5 µg/µL in 10 mM sodium acetate (pH 6.4) until a surface density of approximately 780 resonance units (RU) was reached. Any unreacted active sites were quenched with 1 M ethanolamine (pH 8.5) for 300 s at a flow rate of 10 µL/min. To eliminate non-covalently bound proteins, the sensor chip was washed with HBS buffer for 600 s, followed by a 90-s wash with 120 mM glycine (pH 2.5). The binding affinities were determined using WAVEcontrol software (v.3.1.4.4, Malvern) by calculating the association and dissociation rate constants based on a simple 1:1 Langmuir interaction model [22] (Supplementary File-S2).

Loading M1A and AS1411

To load AS1411 and M1A into exosome, exosome of varying concentrations were mixed with AS1411 (10 µM) and M1A (1:1000, v/v) derived from CdSe/ZnS core–shell quantum dots based dye (using different colors to seperate them). The mixture was prepared in Axygen™ Disposable V-Bottom Reagent Reservoirs (5 ml) containing 300 µL of electroporation buffer at 4°C. Electroporation was then performed at 400 V and 150 µF using an MSE PRO Gene Electroporator (Tucson, AZ, USA). Following electroporation, the mixture was incubated at 37°C for 30 min to ensure complete recovery of the exosome plasma membrane. To remove any unbound exosomes, the final product, termed AP-BEV + M1A-EXO, was washed twice with cold PEGylated (1.5% w/w) PBS by ultracentrifugation at 4000 rpm for 90 min. The payload of M1A and AS1411 within the exosome was determined based on the fluorescence of M1A and AS1411 (λ = 500 nm) using Agilent 8453 G1103A Spectrophotometer.

Experimental evaluation of NDDS

The particle size, polydispersity (PDI), particle charge, and surface morphologies, of BEV-API, BEV-PM, AP-BEV + M1A-EXO, and BEV-CHI-NP were examined using DLS (Zetasizer Ultra, Malvern, Waltham, MA, USA) and scanning electron microscopy (SEM) (Zeiss EVO 40, Oberkochen, Germany) respectively. Differential scanning calorimetry (DSC) and transmission electron microscopy (TEM) (HT7800, Hitachi High-Tech America were employed to map the elemental composition of the samples.

Chromatographic and Mass Spectrometry Setup

BEV was obtained from SelleckChem, with careful consideration given to the CDR (Heavy chain: RFTFSLDTSKSTAYLQMNSLR), as this information is crucial for selecting the appropriate SIL peptide [23]. Consequently, SILu™-MAb, with the FTFSLDTSK region (*labeled with*

Arginine-$^{13}C_6$, $^{15}N_4$ and Lysine $^{13}C_6$, $^{15}N_2$), was used as the internal standard, synthesized by Sigma Aldrich, based on the findings of Iwamoto *et al*. [23]. The LC–MS conditions were set as follows: solvent A consisted of 0.1% aqueous formic acid (FA), while solvent B was acetonitrile (ACN) with 0.1% FA The chromatographic separation was performed using Shim-pack GIST C18, 2 µm, 2.1 × 150 mm from Shimadzu (Drive Columbia, MD, USA), at a column temperature of 30°C and a flow rate of 0.3 ml/min. The gradient program was as follows: 0–5 min: %B = 3, 5–45 min: %B = 3–30 gradient, 45–56 min: %B = 95, 56–65 min: %B = 3. MS and MS/MS spectra were acquired with a desolvation line temperature of 300°C and a heat block temperature of 300°C. The nebulizer nitrogen gas flow rate was 1.5 ± 0.1 L/min, with a drying gas pressure of 80 kPa. Ion accumulation times were set at 20 ms for MS and 60 ms for MS/MS analysis. MS/MS analysis was conducted in automated data-dependent mode with collision-induced dissociation cell electrode voltage of −1.3 V.

Stock solutions were prepared in methanol and stored at − 20°C. Calibration curves for each peptide were established by preparing plasma samples with BEV concentrations ranging from 0.146 to 300 µg/ml, using a twofold serial dilution to create nine calibration points. The lower limit of quantification (LLOQ) was set at 0.292 µg/ml, while the low, middle, and high quality control (LQC, MQC, HQC) concentrations were set at 0.584, 5, and 150 µg/ml, respectively. The run acceptance criteria were defined according to ICH M10 guidelines and the Bioanalytical Method Validation Guidance for Industry [24]. An analytical run was considered valid if at least four out of six QC results, and at least one of the two QC replicates at each concentration level, fell within 20% of their nominal values. Validation data was shared as a Supplementary File-S2.

Stability Testing Under Controlled Conditions

The stability of the formulations was assessed under both long-term (25°C/60% RH) and accelerated (40°C/75% RH) conditions following the ICH Q1A(R2) guidelines [25]. A Binder KBF-S 115 Humidity Test Chamber (3.6 Cu. Ft, Binder, Camarillo, CA, USA) was used to maintain precise temperature and humidity levels throughout the study. Samples of AP-BEV + M1A-EXO and BEV-CHI-NP formulations were stored in sealed containers within the chamber for up to six months. At predefined intervals (0, 1, 3, and 6 months), aliquots were retrieved and analyzed for encapsulation efficiency (%EE), particle size, and zeta potential. Encapsulation efficiency was determined using validated UV–Vis spectrophotometry, while particle size and zeta potential were measured using dynamic light scattering (DLS). Physical changes, such as aggregation, were documented visually and through microscopy to provide a comprehensive evaluation of formulation stability under the specified conditions.

Drug Release Kinetics in Controlled Environments

BEV Release

The release profile of BEV from BEV-API, BEV-PM, BEV-CHI-NP, and AP-BEV + M1A-EXO formulations was evaluated under varying pH conditions over time. To mitigate drug-induced hydrophobicity, each formulation was prepared with 25 mg/mL of BEV, and the solution pH was adjusted to 7.4. For BEV-PM and BEV-CHI-NP, the formulations were prepared in 5 mL vials and incubated in a water bath at 37°C with a rotation speed of 50 rpm [26]. At specific time intervals up to 8 days, 3 mL of the buffer solution was replaced with fresh buffer at the corresponding Ph,7.4. The concentration of BEV in each sample was determined using LC–MS/MS method that described in *Chromotographic settlement*. To investigate the release mechanism, the *in vitro* release profiles were compared against three different kinetic models based on established methodologies.

AS1411 and M1A Release

The release profiles of the AS1411 aptamer and M1A-loaded mRNA from the AP-BEV + M1A-EXO formulation were studied under controlled conditions. The formulation was placed in dialysis bags with a molecular weight cutoff of 3.5 kDa, which were immersed in 10 mL of release medium (PBS, pH 7.4, or acetate buffer, pH 5.5) at 37°C with gentle stirring at 100 rpm. These conditions were selected to replicate physiological and acidic tumor environments.

At predetermined time intervals (8, 24, and 48 h, and up to 7 days), 1 mL of the release medium was collected and replaced with fresh buffer to maintain sink conditions. The collected samples were analyzed to determine the concentrations of the aptamer and mRNA. While AS1411 was fluorescently labeled, and its release was measured using a spectrofluorometer by detecting fluorescence at λex = 500 nm and λem = 520 nm, M1A concentrations were quantified using qPCR after extracting RNA from the collected samples [18].

Computational Release Setup

The ADMET predictor software (v8.3.3.1, Simulation Plus Inc., Lancaster, CA, USA) was employed to perform an in silico simulation of the absorption, distribution, metabolism, and excretion (ADME) of BEV-API, BEV-PM, AP-BEV + M1A-EXO, and BEV-CHI-NP across plasma and key organs such as the brain, liver, heart, and kidneys.

This software uses a conceptual approach, leveraging *in vitro/in vivo* data from various compounds to build predictive models through Machine Learning (ML). Mathematical and statistical methods were utilized to correlate the effective permeability of the formulations with their calculated molecular descriptors. Given that BEV is a monoclonal antibody (mAb), eight specific descriptors were used, including kD, His, measured pI, calculated pI, sedimentation coefficient (s), effective charge (z*) at pH 6.0, diffusion coefficient (D), weak cation exchange (WCX) retention time, and Fab/Fc charge separation parameter (Fab/Fc-CSP) [27]. The simulation replicated a transwell system with endothelial cells from plasma and major organs, with a cell density of approximately 40,000 cells/sq cm. Pharmacokinetic parameters were then predicted focusing on the distribution of the permeated molecules within the plasma and colon.

Molecular Interaction Studies for NDDS

Docking studies were performed using Autodock Vina (v.4.1.1.2, Source Forge, San Diego, CA, USA) to evaluate the binding affinity of BEV, M1A, AS1411, Chitosan, and PDC, which are components of the BEV-API, BEV-PM, AP-BEV + M1A-EXO, and BEV-CHI-NP formulations. The APIs and lipids were sourced from the European Bioinformatics Institute (https://www.ebi.ac.uk/), while protein-based components were obtained from the Protein Data Bank (https://www.rcsb.org/). These components were aligned with the specific cell lines derived from colon cancer mouse model which are cell-surface G-protein-coupled receptors GPR41, GPR43, and GPR109A, phospholipid and cholesterol [28]. The resulting 3D complex structures were then examined using PyMOL (v.3.0.8, Schrodinger, Mannheim, Baden-Wurttemberg, Germany) to identify key hydrogen bond interactions and assess the overall docking poses. Furthermore, 2D interaction diagrams were generated using BIOVIA Discovery Studio 2024 (v.4.6.1.1, Dassault Systems, Waltham, MA, USA) to provide a detailed analysis of the specific amino acid residues within the protein complexes that are involved in binding with the studied compounds.

Organoid Model, Treatment and Survival

3D Cell Growth and Maintenance

Tumor tissue fragment was cut into small ~ 1–2 mm pieces. The tissue fragments were washed 2–3 times with cold PBS solution and then incubated at 4°C in an antibiotic mixture (100 µg/mL Normocin), 50 µg/mL Gentamicin, and 1X Pen/Strep in 1X PBS for 20 min and washed again with cold PBS solution. Tissues are placed in 5 mL of collagenase prepared at a concentration of 0.5 mg/ml for enzymatic dissociation and incubated at 37°C for 30–60 min. Every 10–15 min, the tube was shaken vigorously 10–15 times to aid enzymatic dissociation. After incubation, Culture media was added to stop the enzymatic activity. The suspension was passed through a sterile 70 µm cell strainer and centrifuged at 300 g for 5 min at 4°C. Isolated crypts were then embedded in Matrigel in 1:4 w/w. The matrigel was allowed to polymerize for 10–12 min at 37 oC and then culture media was added. The culture medium was previously prepared with Advanced DMEM, 1X Glutamax, 10 mM HEPES, 50% WRN conditioned medium derived from L-WRN cell line, 1X B27, 1X N2, 10 mM Nicotinamide, 1 mM N-acetyl cysteine, 100 µg/mL Primocin, 10 µM SB202190, 10 µM Y-27632, 10 nM Gastrin I, 50 ng/mL EGF, and 500 nM A83-01. Culture media were refreshed every 2–3 days and organoids were passaged every 8–10 days. Organoids were removed from Matrigel using Cell Recovery Solution (CRS) and then incubated in TryplE Express at 37°C to make single cells and passaged. Cells were cultured as described above.

Treatments

BEV-API, BEV-PM, AP-BEV + M1A-EXO, and BEV-CHI-NP were dissolved in D-PBS. BEV-API was prepared with a final stock concentration of 500 µg/mL (3.35 µM). To provide an equal final BEV-API concentration for each NDDS, which are BEV-PM, AP-BEV + M1A-EXO, and BEV-CHI-NP were prepared as 3500 µg/mL regarding the drug loading ratio (1:7, w/w). Followingly, six different concentrations of BEV-API between 0.1–500 µg/mL (0.67–3355.7 nM) and for NDDSs doses between 0.7–3500 µg/mL in parallel were used for organoid culture assays.

Evaluation of Cytotoxic Effects

Organoid cell viability was analyzed using CellTiter-Glo 3D cell viability reagent optimized for 3D cultures according to the manufacturer's instruction, and luminescence was measured as in our previous study [29]. The results of all groups were normalized to the control group. Half-maximal inhibitory concentration (IC_{50}) values were determined using Excel macro function (v2013, Microsoft, Redmon, WA, USA).

Animal Model Evaluation

Administration and Animal Groups

All animal experiments were approved by the Animal Care Committee of the University of Kentucky Affiliated

Laboratory Animal Division (*Approval No: 2024–1129*). To investigate the effects of BEV-API, BEV-PM, AP-BEV + M1A-EXO, and BEV-CHI-NP on colorectal tumorigenesis, we utilized Heterozygote ApcMin mice on a C57BL/6 background, a model known for spontaneous intestinal tumor formation. Mice were assigned according to the power analysis (*alpha 0.05, power 90% <)* to different treatment groups corresponding to each formulation. The animals were randomly divided into five groups, each consisting of seven mice: (i) BEV-API (free BEV in water), (ii) BEV-PM (iii) BEV-CHI-NP, (iv) AP-BEV + M1A-EXO (v) empty nanoparticle of BEV-PM (vi) empty nanoparticle of BEV-CHI-NP (vii) empty nanoparticle of AP-BEV + M1A-EXO, and (viii) an untreated control group (0.9% saline). Mice receiving BEV formulations were administered a dose of 5 mg/kg body weight intraperitoneally (ip) twice per week (28 days) [30]. Tumor formations were assessed by micro-computed tomography (Micro-CT, SkyScan 1172, Bruker, Billerica, MA, USA).

Pharmacokinetic Evaluation

For the pharmacokinetic assessment, plasma samples were collected at specified time intervals over the course of 28 days to evaluate the drug levels of BEV-API, BEV-PM, AP-BEV + M1A-EXO, and BEV-CHI-NP. Blood samples were obtained via tail vein or retro-orbital sampling at predetermined time points post-administration, including immediately after dosing and at subsequent intervals. The samples were centrifuged to separate the plasma, which was then stored at −80°C until analysis. Plasma concentrations of BEV were quantified using a validated analytical method that explain in proper subtitle (*Chromotographic settlement*), and the pharmacokinetic parameters, including the area under the curve ($AUC_{0\text{-}t}$), half-life ($t_{1/2}$, maximum concentration (C_{max}), and time to reach maximum concentration (T_{max}), were determined for each formulation.

Tissue and Molecular Analysis of Tumor Response

The sections were polished to a final thickness of 30 µm and examined using confocal laser scanning microscopy (Axioscope 5, Zeiss, San Diego, CA, USA) to observe cancer formation. Additionally, sections were embedded in paraffin, sliced into 5 µm sections, and stained with hematoxylin and eosin (modified acc. Gill III) to evaluate anticancer activity.

After the animal study, total RNA was isolated from the cells using TRIzol reagent, with the RNA quality assessed via an RNeasy mini kit and gel electrophoresis (Electrophoresis Chambers, Bio-Rad, Hercules, CA, USA). Complementary DNA (cDNA) was then synthesized using a cDNA Synthesis Kit. Quantitative real-time PCR was performed using QuantStudio 7 (Applied Biosystems, Waltham, MA, USA) with primers and MitoGreen. The GAPDH gene was used as the housekeeping gene, and the relative expression levels of CEA, TYMS, CA 19–9, and CA-125 were calculated using the $2-\Delta\Delta CT$ method, based on thermal cycling conditions.

The most potent formulations, including BEV-API, BEV-PM, AP-BEV + M1A-EXO, and BEV-CHI-NP, were incubated for 72 h with cells isolated from our colon cancer mouse model. Following trypsinization, both untreated and treated cells were stained with annexin V/PI for 15 min. Subsequently, the cells were fixed and incubated with streptavidin-fluorescein (5 µg/mL) for an additional 15 min. The anticancer effect, mediated through apoptosis, was evaluated by quantifying annexin-stained apoptotic cells using the FITC signal detector (FL1) in comparison with the phycoerythrin emission signal detector (FL2).

Tissue Architecture and Cellular Structures

The slides were first incubated at 63°C to melt the paraffin, then transferred to Xylene I followed by Xylene II for 15 min each to remove any residual paraffin. Rehydration of the samples was achieved by dipping them three times in a descending alcohol series: twice in 96% ethanol, followed by 70% ethanol, 40% ethanol, and finally distilled water. Nuclei were stained with Hematoxylin for 8 min, followed by a wash in deionized water. The slides were then placed in tap water for 10 min to allow the staining to develop. Cytoplasmic structures and the extracellular matrix were stained with Eosin for 8 min [31]. Afterward, the samples were dehydrated in an ascending alcohol series, dipping twice in 70% ethanol and twice in 96% ethanol, followed by a 5-min incubation in Isopropanol I, Xylene I, and Xylene II. The samples were mounted using Mount-Quick and sealed with a coverslip. Images were collected using a confocal microscope TCS SP8 (Leica Microsystems, San Diego, CA, USA).

Data Interpretation

Bioactivity and cytotoxicity assays were repeated in quadruple and the results of each experiment were analyzed with one-way ANOVA and Tukey's post hoc tests. The statistical significance was accepted as $p < 0.05$ and determined by GraphPad Prism Software (v.9.0, LaJolla, CA, USA).

Results and Discussion

Characterization of NDDS

The data regarding the DoE was interpreted in Supplementary material-S1. The DLS analysis of the BEV-PM formulation, which integrates BEV with the $PCL_{1000}PEG_{2000}$, reveals a narrow size distribution centered at approximately 205.8 nm (Fig. 2A). This size consistency indicates efficient encapsulation of BEV within the micelle structure formed by the amphiphilic $PCL_{1000}PEG_{2000}$ copolymer. The zeta potential of + 14.4 mV suggests moderate stability due to electrostatic repulsion, sufficient to prevent aggregation under physiological conditions (Fig. 2A). The SEM image (Fig. 2D) confirms the DLS findings by showing smooth, spherical particles typical of well-formed micelles. Such morphology is consistent with findings from recent studies, where polymeric micelles composed of PEG-based copolymers displayed similar characteristics and were noted for their potential in enhancing drug bioavailability [32, 33]. The DLS data for the BEV-CHI-NP formulation, comprising BEV, CHI, and PEG, shows a broader size distribution centered at 251.2 nm, reflecting the influence of chitosan's polymeric nature on particle size (Fig. 2B). The zeta potential of + 37.2 mV, attributed to the cationic CHI, indicates high stability due to strong electrostatic repulsion, a characteristic that is crucial for preventing particle aggregation in biological environments. SEM imaging (Fig. 2E) reveals larger, irregularly shaped particles with rough surfaces, which aligns with chitosan's known behavior. This result is supported by recent publications in the study by Islam *et al*., where CHI-based nanoparticles demonstrated similar morphological features and were noted for their sustained drug release properties due to the polymer's mucoadhesive nature [34].

The AP-BEV + M1A-EXO formulation, which integrates BEV conjugated iPSC-derived exosomes with loaded M1A and AS1411, exhibits a size distribution of around 198.2 nm (Fig. 2C). This size is slightly smaller than BEV-PM and BEV-CHI-NP, which is characteristic of exosome-based formulations that tend to be more compact due to their lipid bilayer structure. The AP-BEV + M1A-EXO formulation is a sophisticated delivery system where BEV is conjugated on the exosome surface and coated with PEG, contributing to the positive zeta potential of + 43 mV. This external modification enhances the exosome's stability and extends its circulation time by providing a steric barrier that prevents opsonization and subsequent clearance by the immune system (Fig. 2F).

Inside the exosome, the AS1411 and M1A aptamers are encapsulated, designed to target intracellular components such as tRNA and mtRNA upon delivery into the target cells. The internalization of these aptamers is crucial for disrupting cellular processes at the nucleic acid level, thereby enhancing the therapeutic efficacy. The exosome's lipid bilayer acts as a protective carrier, ensuring that the aptamers reach their intracellular targets without degradation [35, 36]. Meanwhile, the external BEV, by targeting extracellular receptors like VEGF, provides a dual mechanism of action: disrupting angiogenesis externally while the aptamers function intracellularly. This dual-targeting approach is supported by the observed high zeta potential, indicating that the exosome is well-engineered for both stability and targeted delivery, aligning with recent advances in nanomedicine where exosome-based systems are tailored for multi-modal therapeutic strategies [37]. This is supported by recent studies of Luis le redin *et al*., where BEV-NP have been shown to improve the targeting efficiency and therapeutic outcomes of nanoparticle-based drug delivery systems.

The DSC analysis reveals distinct thermal transitions for each component and formulation (Fig. 2G). The PCL_{1000}-PEG_{2000} copolymer and PCL show melting points at 56.16°C and 61.3°C, respectively, which are indicative of their crystalline structures [38, 39]. CHI exhibits a broad thermal transition around 150.5°C, consistent with its semi-crystalline nature [40]. While BEV-PM formulation displays shifts in thermal transitions, suggesting interactions between BEV and the polymer matrix, which could influence the stability and release profile of the drug, and BEV-CHI-NP formulation shows a thermal event at 100.8°C, indicating the stability of the CHI structure under heating, which is crucial for maintaining the integrity of the loaded PEG and drug during storage and administration.

The AP-BEV + M1A-EXO formulation was not included in the DSC analysis due to the heat sensitivity of its components [41, 42]. Exosomes, particularly those loaded with aptamers like AS1411 and M1A, and proteins like BEV, are known to be highly susceptible to thermal denaturation. Exposure to elevated temperatures during DSC can compromise the structural integrity of the lipid bilayer and denature the nucleic acids and proteins encapsulated or conjugated to the exosome surface [43]. The study conducted by Sulthana *et al*. provided compelling evidence of instability within their exosome-based formulations when subjected to thermal stress because heat can lead to the aggregation and precipitation of exosomal components [44]. Therefore, to preserve the bioactivity and therapeutic potential of the AP-BEV + M1A-EXO formulation, it was excluded from the DSC analysis to avoid degradation that could otherwise compromise its effectiveness in targeted drug delivery applications.

In addition, TEM images provide and support detailed insights into the morphological characteristics of the nanoparticle formulations. Figure 3A shows the BEV-CHI-NP, which appears as relatively uniform, spherical particles with some degree of aggregation. The size and shape observed are consistent with typical chitosan-based nanoparticles

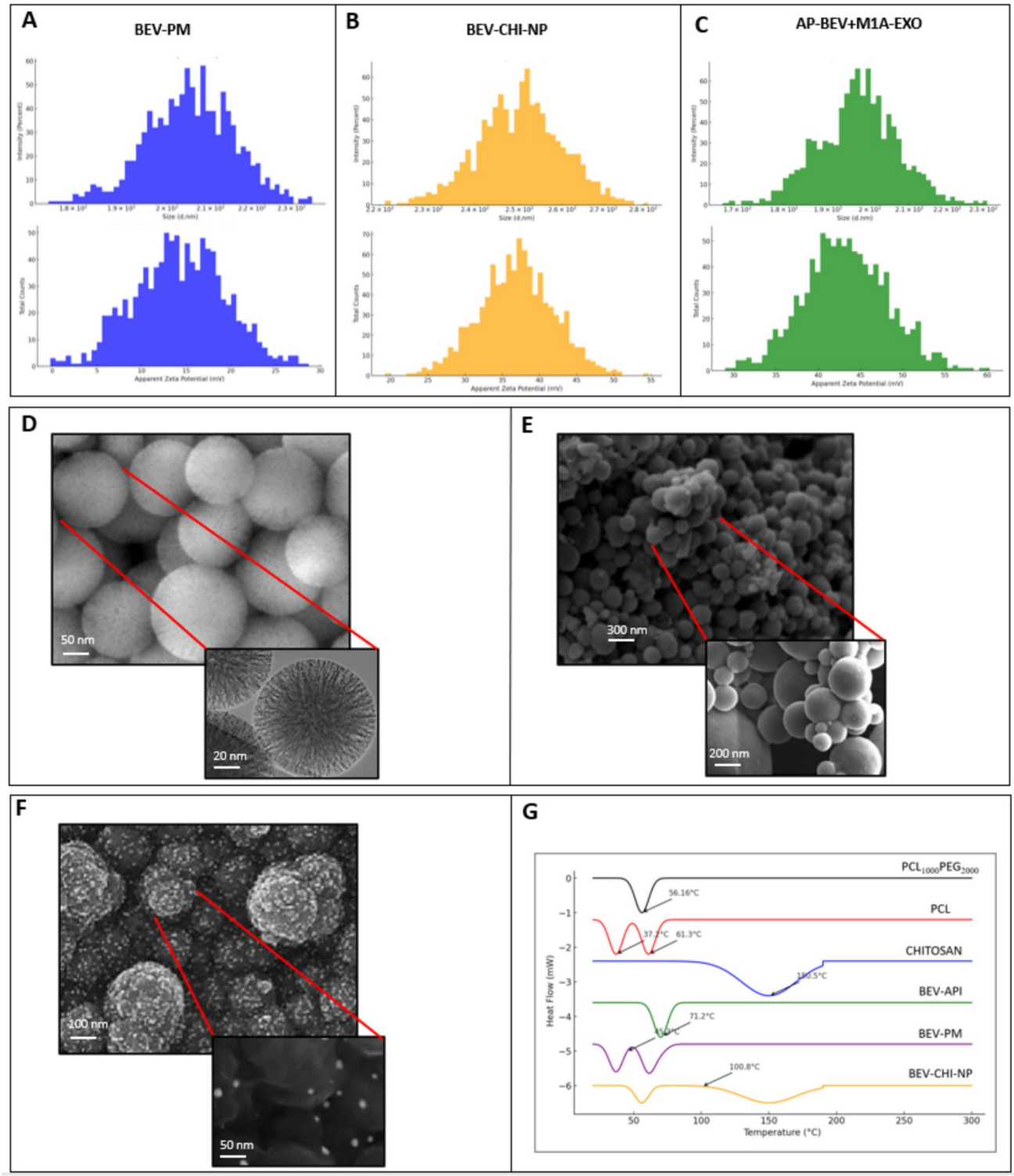

Fig. 2 Structural differences and chemical formation based analysis of the formulations **A** Particle size distribution and zeta potential of BEV-PM, **B** Particle size distribution and zeta potential of BEV-CHI-NP **C** Particle size distribution and zeta potential of AP-BEV + M1A-EXO **D** Morphological characterization of BEV-PM via SEM **E** Morphological characterization of BEV-CHI-NP via SEM **F** Morphological characterization of AP-BEV + M1A-EXO via SEM **G** DSC analysis on various formulations and components, excluding exosome formulation and components

[45], which are known to form larger, more irregular aggregates due to the polymer's natural properties [45, 46].

Figure 3B displays the BEV-PM, which also shows spherical particles but with a more homogeneous distribution and less aggregation compared to BEV-CHI-NP. This uniformity and smaller particle size are likely due to the micelle formation by the PCL_{1000}-PEG_{2000} copolymer, which provides a stable hydrophobic core for drug encapsulation and a hydrophilic shell that enhances solubility and stability in aqueous environments [38, 39]. Regarding the BEV + M1A-EXO formulation, Fig. 3C reveals well-defined, uniformly sized exosomes with minimal aggregation, a characteristic that is essential for maintaining the integrity and functionality of the exosomes in drug delivery [47, 48]. Exosomes are naturally occurring vesicles with a lipid bilayer, which is preserved during the loading and conjugation processes, as shown by the clear and consistent morphology. Goetzl *et al.* conducted a study regarding the minimal aggregation feature

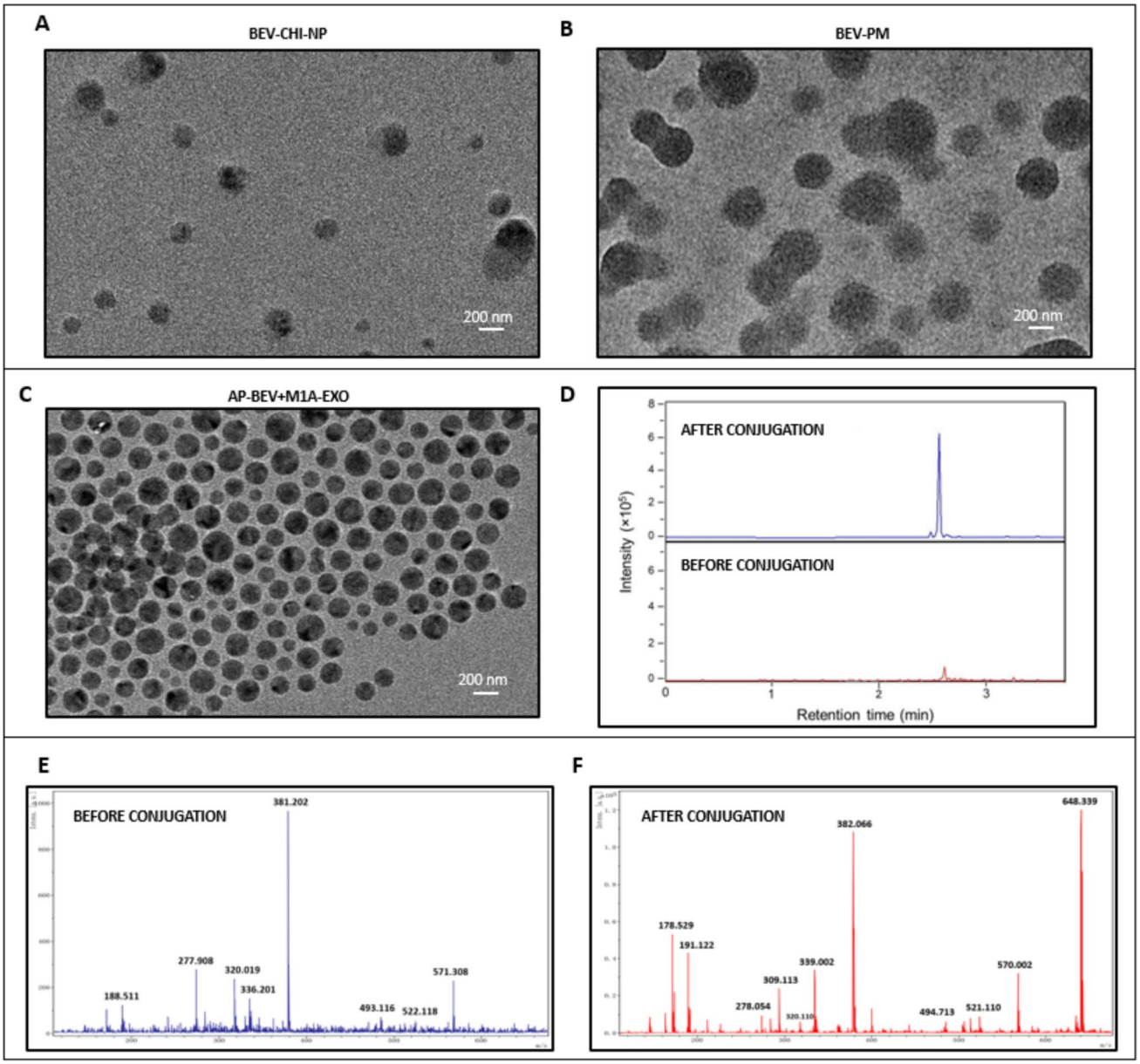

Fig. 3 Morphological and quantitative analysis of formulations **A** Particle size distribution and zeta potential of BEV-PM, **B** Particle size distribution and zeta potential of BEV-CHI-NP **C** Particle size distribution and zeta potential of AP-BEV + M1A-EXO **D** Morphological characterization of BEV-PM via SEM **E** Morphological characterization of BEV-CHI-NP via SEM **F** Morphological characterization of AP-BEV + M1A-EXO via SEM **G** DSC analysis on various formulations and components, excluding exosomal formulation and components

of the exosome, which highlights the potential of exosomes as stable and effective carriers for targeted drug delivery, particularly when modified with aptamers and therapeutic proteins [43].

The mass spectroscopy results, as shown in Fig. 3D, E, and F, are specifically focused on the analysis of the exosome formulation AP-BEV + M1A-EXO before and after the conjugation of BEV. Figure 3D illustrates a significant increase in signal intensity after conjugation, indicating the successful attachment of BEV to the exosome surface. The mass spectra in Fig. 3E and F reveal distinct peaks corresponding to the molecular components of the exosomes. Before conjugation, the spectrum predominantly shows peaks associated with the exosome's intrinsic proteins and nucleic acid cargo, such as M1A and AS1411 aptamers. After conjugation, new peaks appear at higher molecular weights, confirming the presence of BEV on the exosome surface. The shift in the mass spectra and the emergence of these new peaks post-conjugation provide clear evidence that BEV has been successfully conjugated without compromising the structural integrity of the exosomes [49, 50]. Goetzl *et al*. also conducted the study, highlighting that successfully conjugating therapeutic agents to exosomes can significantly enhance their targeting capabilities and therapeutic efficacy while maintaining their stability and functional properties [43].

Release study

The validation of the LC–MS/MS method for BEV was conducted comprehensively across multiple parameters, ensuring the method's robustness and reliability. The calibration curves for both plasma and PBS demonstrated strong linearity, with correlation coefficients (R^2) of 0.99 and 0.98, respectively. These high R^2 values indicate that the method can accurately quantify BEV across a wide range of concentrations, making it suitable for both biological and buffer matrices.

The Limit of Detection (LOD) and Limit of Quantification (LOQ) values further underscore the method's sensitivity. In plasma, the LOD was determined to be 0.750 ng/mL, and the LOQ was 0.00133 µg/mL. For PBS, the LOD was slightly lower at 0.65 ng/mL, with an LOQ of 0.0021 µg/mL. These values demonstrate that the method can reliably detect and quantify even minute concentrations of BEV, which is crucial for applications requiring high sensitivity, such as pharmacokinetic studies [24]. The accuracy and precision of the method were validated through both intra-day and inter-day analyses. The results showed %CV values below 5% across all quality control levels, confirming the method's reproducibility. The slight discrepancies observed between the predicted and obtained concentrations further highlight the method's robustness, as these variations remained within acceptable limits, ensuring that the method consistently delivers accurate results. Recovery rates were high, exceeding 98% across different concentration levels, which indicates that the extraction and quantification processes are highly efficient with minimal analyte loss. Stability studies, including short-term, long-term, and freeze–thaw assessments, demonstrated that the method maintains consistent performance under various storage and handling conditions. This narrow range suggests that the repeatability of the method is excellent, with most data points falling within ± 1.5% of the mean (Supplementary File-S2).

The *in vitro* release profiles of BEV from various formulations were rigorously analyzed using multiple kinetic models, including Zero-order, Higuchi, Korsmeyer-Peppas, 1st-order, and Weibull models. The R^2 values provided critical insights into the fitting of each model to the experimental data, elucidating the underlying mechanisms of drug release.

Figure 4A represents the cumulative release profile of BEV from the EXO formulation under standard pH conditions. The release mechanism was designed to allow for the controlled detachment of BEV from the exosomal carrier at the target site, ensuring its bioavailability and therapeutic efficacy. Studies under varying pH conditions were conducted separately to evaluate stability and release behavior under physiological and pathological environments. The AP-BEV + M1A-EXO formulation exhibited the highest Zero-order release rate constant, indicative of a controlled release pattern likely attributed to the exosome's lipid bilayer, which modulates the diffusion of BEV.According to recent literature, *in vitro* release studies highlight the potential of exosome-based drug delivery systems for achieving sustained and controlled release [51, 52]. In contrast, the BEV-CHI-NP formulation demonstrated a lower Higuchi rate constant, reflecting the diffusion-limiting properties of chitosan, a polymer known for forming dense matrices that retard drug diffusion (Fig. 4A). Desai *et al*. similarly reported that CHI matrices significantly decelerate the release of large biomolecules, supporting our findings [53].

The Korsmeyer-Peppas model provided the best fit for all formulations, as indicated by the highest R^2 values. The AP-BEV + M1A-EXO formulation, in particular, showed an elevated release rate constant in this model ($p < 0.05$), suggesting a complex release mechanism involving both diffusion and exosome membrane degradation (Fig. 4A). The n values approaching 0.8 across formulations suggest that the release is governed by a combination of diffusion and matrix erosion, in line with the release behavior of polymeric nanoparticles documented in recent studies [54, 55]. The First-order kinetic model, which posits that the release rate is concentration-dependent, was more applicable to BEV-PM and BEV-CHI-NP formulations. However, the relatively lower R^2 values suggest that while concentration influences release, it is not the dominant factor. The Weibull model, known for describing release

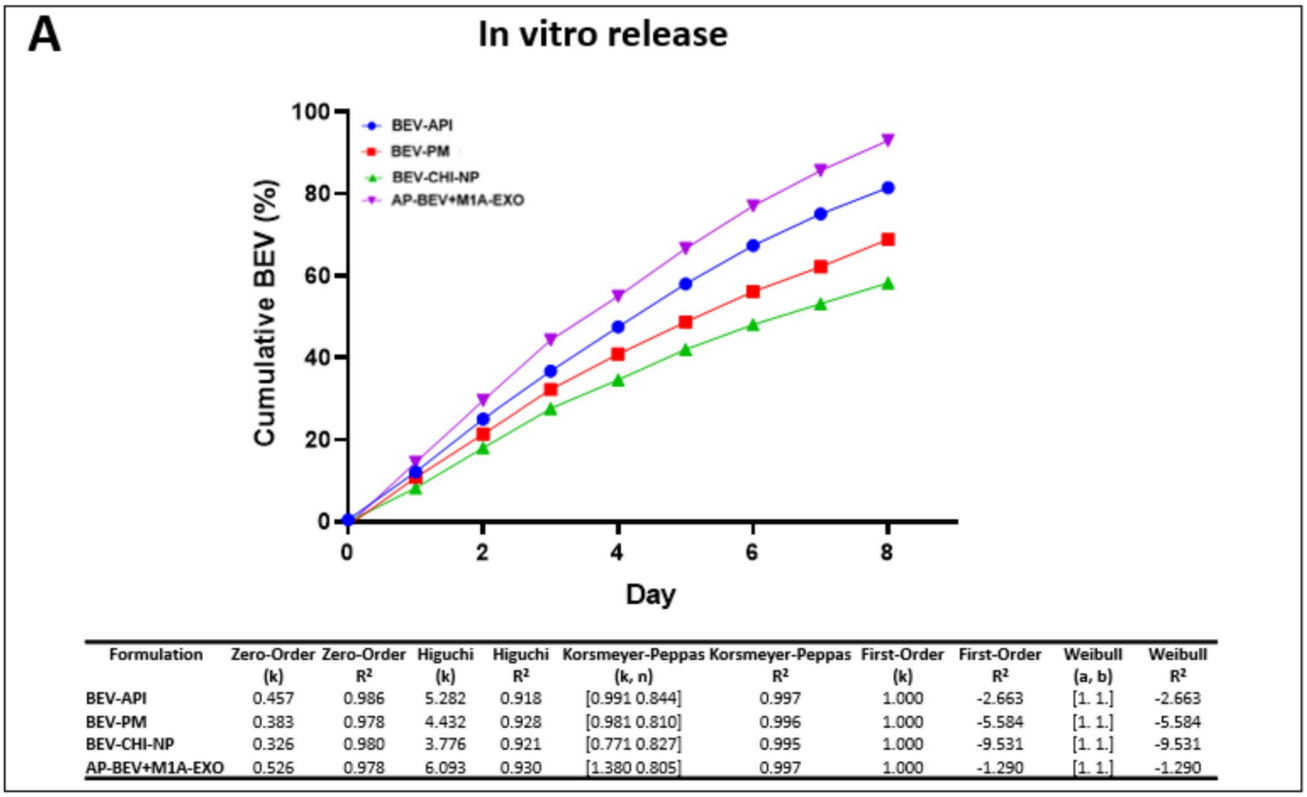

Formulation	Zero-Order (k)	Zero-Order R^2	Higuchi (k)	Higuchi R^2	Korsmeyer-Peppas (k, n)	Korsmeyer-Peppas R^2	First-Order (k)	First-Order R^2	Weibull (a, b)	Weibull R^2
BEV-API	0.457	0.986	5.282	0.918	[0.991 0.844]	0.997	1.000	-2.663	[1. 1.]	-2.663
BEV-PM	0.383	0.978	4.432	0.928	[0.981 0.810]	0.996	1.000	-5.584	[1. 1.]	-5.584
BEV-CHI-NP	0.326	0.980	3.776	0.921	[0.771 0.827]	0.995	1.000	-9.531	[1. 1.]	-9.531
AP-BEV+M1A-EXO	0.526	0.978	6.093	0.930	[1.380 0.805]	0.997	1.000	-1.290	[1. 1.]	-1.290

Fig. 4 *In Vitro* and in silico release profiles of BEV **A** *In vitro* release and kinetic model analysis in pH 7.4 **B** In silico predicted release and distribution of BEV in plasma and major organs **C** In silico compartment-based distribution **D** In silico ADME descriptor analysis for BEV formulations

from complex systems, provided an excellent fit for the AP-BEV + M1A-EXO formulation, indicating that multiple mechanisms, including diffusion, degradation, and component interactions, contribute to the release process.

Graphically, the AP-BEV + M1A-EXO formulation displayed the most rapid and extensive release, nearing complete release within the study period. This accelerated release can be attributed to the exosome's ability to efficiently encapsulate and deliver its payload, as supported by findings from Johnsen *et al*. (2022). Conversely, the BEV-CHI-NP formulation exhibited the slowest release, which is consistent with the known diffusion-restrictive properties of CHI matrices. This behavior is in agreement with the Higuchi model and is corroborated by studies such as those by Kar *et al*. [56], which reported that chitosan-based nanoparticles provide prolonged drug release.

The BEV-PM formulation, utilizing a PCL_{2000}-PEG_{1000} copolymer, exhibited a moderate release rate. The PEGylation likely contributes to a balanced release, enhancing solubility and reducing protein aggregation, thereby ensuring a controlled release profile.

The predicted in silico data suggested that BEV-API and BEV-PM formulations demonstrated higher permeability in plasma and the liver, attributed to their relatively stable molecular structures and optimized diffusion coefficients (Fig. 4B and D). The AP-BEV + M1A-EXO formulation, which incorporates exosomes, showed enhanced distribution to the brain and heart, likely due to the exosome's ability to traverse biological barriers more effectively, including the blood–brain barrier (BBB) (Fig. 4B). This aligns with recent studies suggesting that exosome-based delivery systems can enhance the central nervous system (CNS) uptake of therapeutic agents [57, 58].The AP-BEV + M1A-EXO's lipid bilayer structure provides protection to the payload while enabling controlled release in response to environmental triggers, such as pH changes in the tumor microenvironment. Studies have shown that exosomes facilitate enhanced uptake and release through receptor-mediated endocytosis and fusion with target cell membranes, thereby ensuring efficient payload delivery [59, 60].

In contrast, the BEV-CHI-NP formulation exhibited lower permeability across all organs, particularly in the brain, which is consistent with the slower release profile observed in experimental studies (Fig. 4B). The liver and kidney distribution profiles observed in Fig. 4B highlight significant differences between the nanoparticle formulations. The

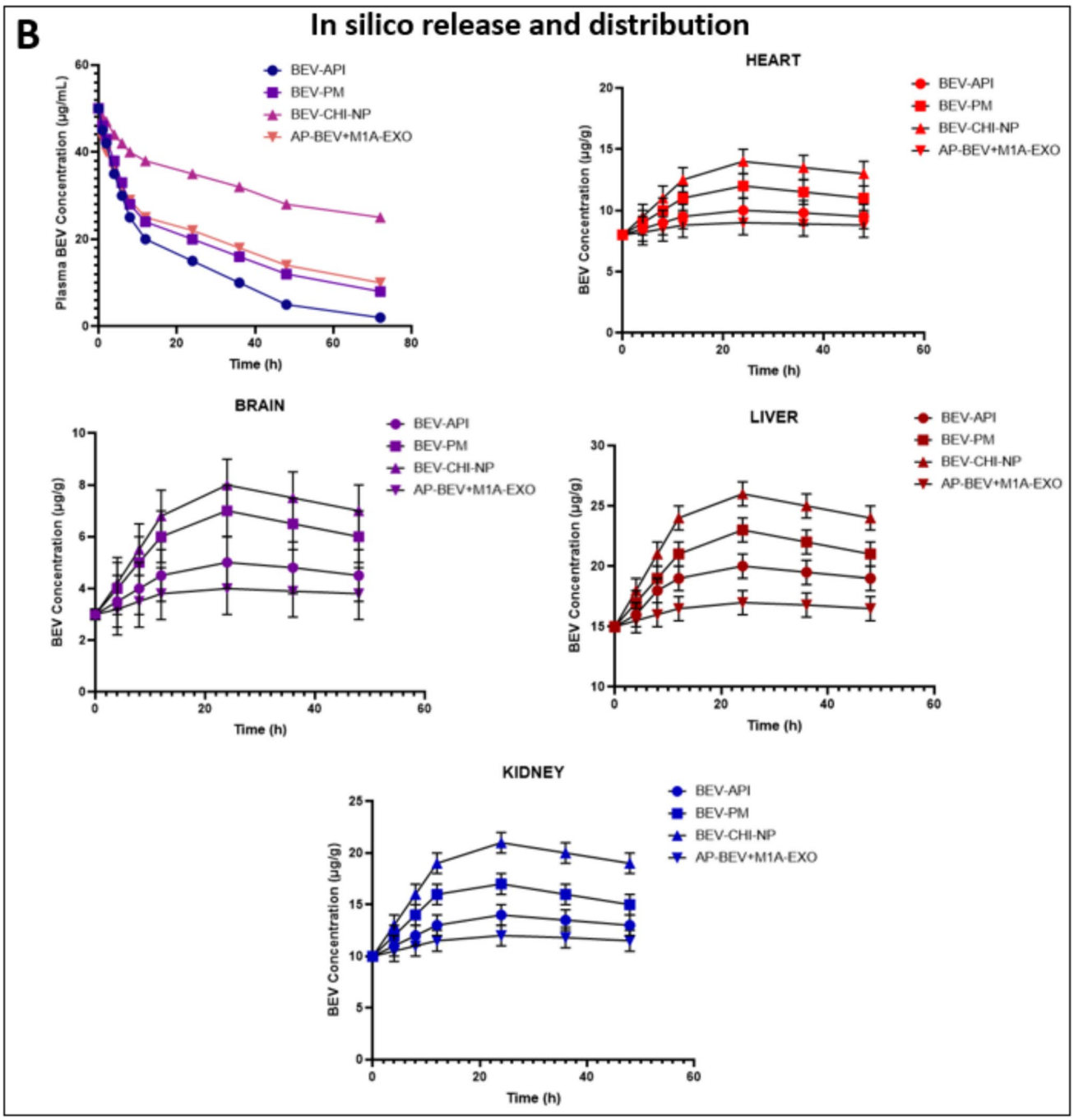

Fig. 4 (continued)

AP-BEV + M1A-EXO formulation exhibited higher accumulation in the liver compared to BEV-CHI-NP and BEV-PM, likely due to its exosomal nature and lipid bilayer structure, which facilitates interactions with hepatic Kupffer cells. This aligns with literature suggesting that exosome-based formulations are preferentially taken up by the mononuclear phagocyte system (MPS) in the liver, enhancing biodistribution but potentially limiting systemic circulation [61]. Conversely, BEV-CHI-NP demonstrated prolonged retention in the kidney, which may be attributed to the chitosan matrix's mucoadhesive properties and its interaction with renal clearance pathways. Chitosan-based nanoparticles are known to exhibit limited biodegradation, potentially leading to slower renal excretion and extended kidney retention, as supported by [62]. This difference in organ distribution is crucial when considering toxicity and therapeutic efficacy,

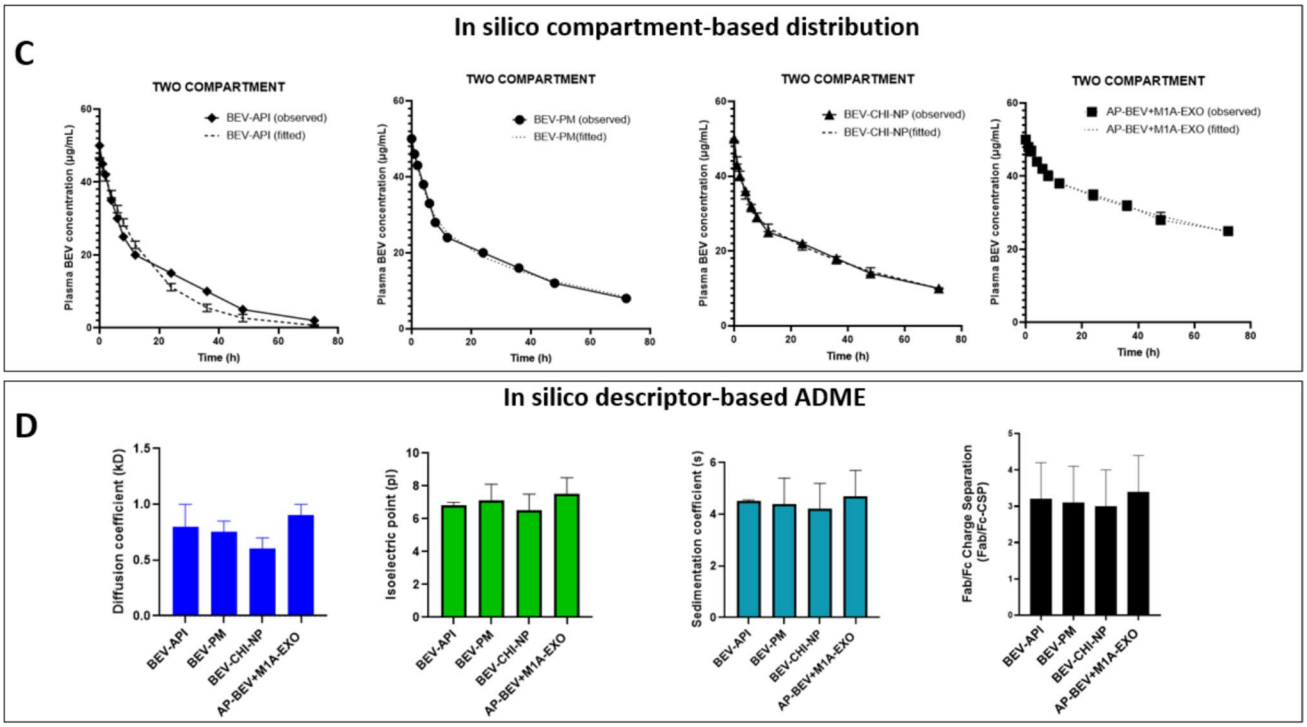

Fig. 4 (continued)

as high liver uptake could lead to hepatotoxicity, whereas renal accumulation requires careful monitoring for nephrotoxicity. However, the BEV-CHI-NP formulation showed a more prolonged retention time in the colon, suggesting its potential for targeted therapies requiring sustained release in the gastrointestinal tract.

In pharmacokinetic models, drug concentrations in organs often do not reach zero within the observed time frame due to several factors. Slow elimination is a key factor, particularly in formulations like BEV-CHI-NP or AP-BEV + M1A-EXO, which are designed for gradual, sustained drug release (Fig. 4C). This controlled release maintains detectable drug levels in organs for an extended period. Additionally, in a two-compartment model, the drug can re-distribute between the plasma and tissues, preventing concentrations from dropping to zero. The long elimination $t_{1/2}$ of certain formulations, especially in the beta phase, also contributes to the persistence of drug levels. Furthermore, drugs like BEV, which are often highly bound to plasma proteins, are cleared more slowly, with protein binding acting as a reservoir that gradually releases the drug back into circulation [63, 64](Fig. 4C and D). The stability provided by exosome and nanoparticle formulations further enhances the drug's resistance to rapid degradation and clearance, sustaining drug levels in organs over time. These factors collectively explain why organ concentrations do not drop to zero quickly in pharmacokinetic studies, especially for formulations designed for extended release or targeted delivery.

AP-BEV + M1A-EXO formulation significantly influences its pharmacokinetic behavior, enhancing its ability to target and accumulate in specific tissues, particularly in the brain and tumor areas. This is likely due to the components' ability to interact with intrinsic cellular components such as tRNA and mRNA, promoting more efficient cellular uptake and retention [65]. In contrast, the BEV-CHI-NP formulation, with its CHI-based matrix, exhibited slower release and lower organ permeability, which is beneficial for applications requiring sustained release over extended periods, particularly in the colon.

Lastly, after using in silico software, pharmacokinetic analysis was also obtained for the formulations. It reveals notable differences in drug distribution, clearance, and half-life, reflecting the impact of their specific components on the drug's behavior within the body. BEV-PM, characterized by PEGylation, exhibits a moderate volume of distribution (Vd = 1794.55 L) and clearance (Cl = 331.77 L/h), with a relatively short alpha-phase $t_{1/2}$ of 3.75 h and a prolonged beta-phase half-life of approximately 41.91 h. This suggests a balanced profile that enhances circulation time while maintaining a steady elimination rate. The exosome-based AP-BEV + M1A-EXO formulation shows the highest

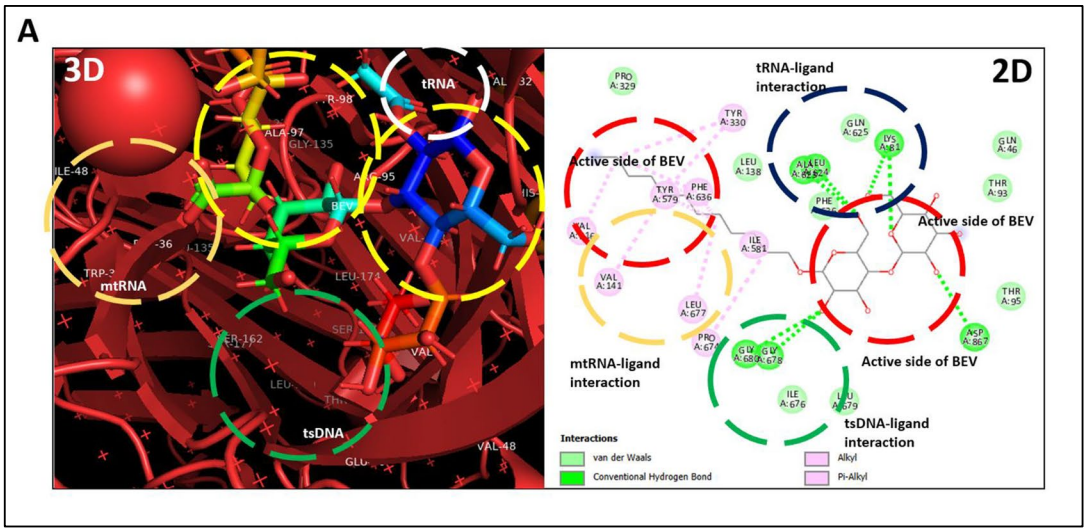
A
3D
tRNA
mtRNA
tsDNA
BEV
2D
tRNA-ligand interaction
Active side of BEV
mtRNA-ligand interaction
tsDNA-ligand interaction
Interactions
van der Waals
Conventional Hydrogen Bond
Alkyl
Pi-Alkyl

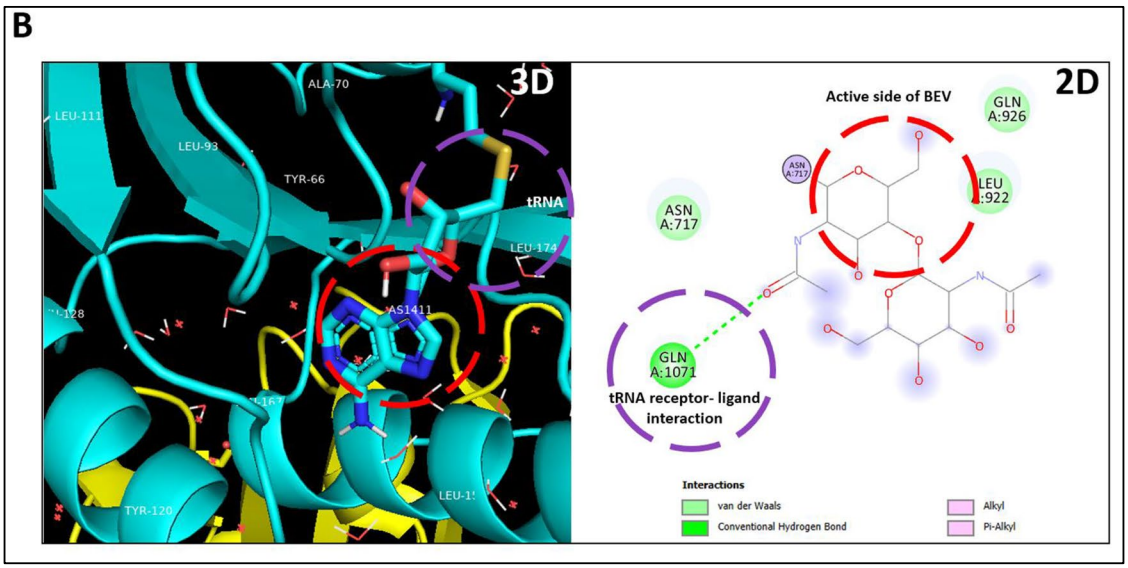
B
3D
tRNA
2D
Active side of BEV
GLN A:926
ASN A:717
LEU A:922
GLN A:1071
tRNA receptor- ligand interaction
Interactions
van der Waals
Conventional Hydrogen Bond
Alkyl
Pi-Alkyl

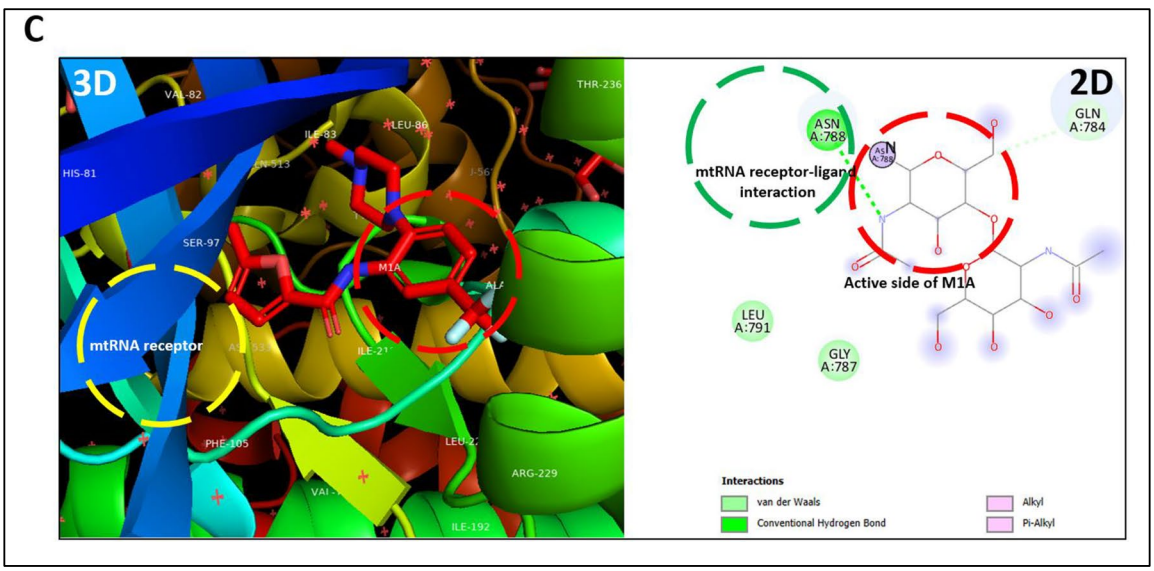
C
3D
mtRNA receptor
2D
mtRNA receptor-ligand interaction
Active side of M1A
ASN A:788
GLN A:784
LEU A:791
GLY A:787
Interactions
van der Waals
Conventional Hydrogen Bond
Alkyl
Pi-Alkyl

◂**Fig.5** 3D and 2D visualization of key binding sites and interactions **A** Molecular docking analysis of BEV interactions with tRNA, mtRNA, and tsDNA **B** Molecular docking analysis of BEV interactions with AS1411 aptamer and BEV interactions with tRNA receptor sites **C** Molecular docking analysis of M1A ligand interaction with mtRNA receptor

volume of distribution (Vd = 5892.26 L) and clearance (Cl = 1133.69 L/h), with a rapid initial distribution phase (alpha half-life of 3.60 h) followed by an extended beta-phase half-life of nearly 99.88 h.

These properties indicate the exosome's ability to enhance tissue penetration and retention, prolonging the drug's activity. BEV-CHI-NP, incorporating chitosan nanoparticles, has a slightly higher volume of distribution (Vd = 2036.35 L) and clearance (Cl = 577.47 L/h) compared to BEV-PM, with a quick alpha-phase t1/2 of 2.44 h and a sustained beta-phase half-life of 44.21 h, likely due to CHI's mucoadhesive properties that enhance tissue interaction. In contrast, BEV-API, the base formulation, displays the lowest volume of distribution (Vd = 781.53 L) and clearance (Cl = 46.5 L/hour), with identical α and bβ $t_{1/2}$ of 11.65 h, indicating a slower and more confined distribution largely within the plasma. These results are associated with real data from Ferreira *et al*.'s study group. They have been researching the impact of conjugated apoptosis on the PKPD data. [66]

Stability Outcomes of Nanoparticle Formulations

The stability assessment of all formulations under long-term (25°C/60% RH) and accelerated (40°C/75% RH) conditions revealed distinct trends over six months. For the AP-BEV + M1A-EXO formulation, %EE decreased slightly but remained above 81% under accelerated conditions, while particle size increased modestly, suggesting slight aggregation as indicated by a reduction in zeta potential (Supplementary file-S3) [41, 67]. The BEV-CHI-NP formulation exhibited a similar trend, with %EE dropping to approximately 76% and noticeable size increases under accelerated conditions, indicating moderate aggregation. In comparison, the BEV-PM micelle formulation maintained relatively high %EE at 82% and exhibited a consistent size increase, reflecting structural changes but still retaining colloidal stability. Overall, all formulations demonstrated good stability under long-term storage, with gradual changes in %EE, size, and zeta potential under accelerated conditions, highlighting their robustness while identifying areas for optimization to enhance performance under extreme storage conditions.

Computational Interaction of Molecules

The docking analysis presented in the 3D and 2D interaction diagrams reveals the intricate binding interactions between BEV and various molecular targets, including tRNA, mtRNA, and tsDNA (Fig. 5A). In the 3D representation, BEV is seen interacting with key residues such as Ala97, Gly135, and Ser152, which are crucial for its binding affinity to the nucleic acid structures. The presence of van der Waals forces, as indicated by the green interactions in the 2D diagram, suggests that these non-covalent interactions play a significant role in stabilizing the BEV-tRNA and BEV-mtRNA complexes. The hydrogen bonding, marked by dotted lines, further enhances the specificity of BEV towards its active sites on these molecular targets. The proximity of residues like Leu138 and Val141 to the active site of BEV indicates a strong interaction with tsDNA, which may contribute to the overall binding efficiency. Additionally, the presence of alkyl and pi-alkyl interactions, highlighted in pink, suggests a potential stacking effect that further stabilizes these complexes [68]. This docking analysis underscores the multifaceted nature of BEV's interaction with cellular components, highlighting its potential efficacy in targeting multiple pathways within the cell, particularly those involving tRNA and mtRNA, which are critical for protein synthesis and mitochondrial function. The comprehensive binding profile depicted here aligns with recent findings that emphasize the importance of such interactions in enhancing the therapeutic potential of monoclonal antibodies like BEV.

On the other hand, the binding interactions between the AS1411 aptamer, BEV, and tRNA receptor sites (Fig. 5B). The 3D visualization highlights the close proximity and interaction between AS1411 and key residues within the tRNA receptor, including Leu111, Tyr66, and Ala70, which play a crucial role in the stabilization of the ligand-receptor complex. The 2D diagram further elaborates on these interactions, revealing the presence of van der Waals forces, conventional hydrogen bonds, and pi-alkyl interactions that contribute to the binding affinity of AS1411 and BEV to the receptor [69, 70]. Notably, residues such as Gln1071 and Asn717 form hydrogen bonds with AS1411, enhancing the specificity of the interaction, while the active site of BEV is shown to engage with Leu922 and Gln926 through van der Waals interactions. These findings suggest a strong and stable binding of AS1411 and BEV to the tRNA receptor, potentially enhancing the therapeutic efficacy of the formulation by effectively targeting the receptor sites and influencing downstream molecular pathways. The detailed interaction map supports the hypothesis that AS1411, when conjugated with BEV, may improve the delivery and efficacy of the therapeutic agent, consistent with recent studies

demonstrating the effectiveness of aptamer-based targeting strategies in drug delivery systems.

Regarding the molecular interactions between the M1A ligand and the mtRNA receptor, 3D visualization highlights key residues involved in stabilizing the M1A binding, such as Ser97, Ile83, and His81, which form a network of interactions around the ligand (Fig. 5C). The 2D diagram further details these interactions, showing the presence of van der Waals forces and conventional hydrogen bonds that contribute to the overall binding stability. Specifically, Asn788 plays a significant role in forming hydrogen bonds with M1A, enhancing the specificity of the interaction with the mtRNA receptor. Additionally, alkyl and pi-alkyl interactions are observed with residues like Leu791, providing further stabilization of the M1A ligand within the active site. These interactions suggest that M1A is effectively targeted to the mtRNA receptor, potentially influencing mitochondrial function. This is consistent with recent studies that have demonstrated the effectiveness of such targeted interactions in modulating cellular processes at the mitochondrial level, thereby offering potential therapeutic advantages in targeting mitochondrial dysfunctions.

Tumor Efficacy of the Formulations in 3D Organoid Culture

AP-BEV + M1A-EXO demonstrated the most potent anticancer activity among NDDSs. According to the CellTiter-Glo 3D viability assay results, BEV-API exhibited an IC_{50} value above the highest tested dose, 500 µg/mL in human colon tumor organoids (HCTO) for 48-h exposure. On the other hand, AP-BEV + M1A-EXO and BEV-CHI-NP showed a potent inhibitory effect on the viability of HCTO, with IC_{50} values 537.8 ± 15.2 and 633.0 ± 23.0 µg/mL, respectively (Table I). Interestingly, BEV-PM did not exhibit a cytotoxic response in HCTO in a time or dose-dependent manner (Fig. 6A). The lack of a cytotoxic response for the BEV-PM formulation, despite its demonstrated antitumor efficacy in Fig. 6**,** can be attributed to its mechanism of action. BEV exerts its therapeutic effects by inhibiting VEGF, thereby suppressing angiogenesis and tumor growth rather than directly inducing cytotoxicity. The polymer matrix in BEV-PM facilitates a sustained and localized release of BEV, enabling effective VEGF blockade at the tumor site without causing significant cellular damage. This aligns with the non-cytotoxic mechanism of VEGF inhibition, which primarily disrupts tumor vascularization rather than directly killing cancer cells. In terms of exosome formulation, AP-BEV + M1A-EXO exhibited the lowest IC_{50} values in both the day 7 and day 8 assays, demonstrating the most potent cytotoxic profile compared to BEV-API and the other treatment groups (Fig. 6A-C). In addition, longer exposure to BEV-CHI-NP up to 6 days exhibited lower anticancer activity in HCTO compared to BEV-API with a slightly higher IC_{50} value as 336.4 ± 20.8 µg/mL, due to a probable degradation of chitosan NP (Fig. 6B.). The degradation of chitosan nanoparticles after 6 days, which results in a decreased pharmacological effect, can be explained by several factors. Enzymatic activity, particularly from lysozyme present in biological systems, can degrade chitosan, compromising the nanoparticles' structural integrity [71, 72]. Additionally, chitosan's pH sensitivity, especially in acidic environments, may lead to increased solubility and faster degradation. Interactions with proteins and other components in biological fluids can also destabilize the nanoparticles. Hydrolysis in aqueous environments further contributes to the breakdown of CHI chains. Moreover, if the nanoparticles are cross-linked, the weakening or loss of these cross-links over time can lead to disintegration [62, 71]. Microscopic examination of HCTOs exposed to the NDDSs for 48-h and 6-days of exposures were also shown in Fig. 7**.**

medium.

Animal Study

Pharmacokinetic Evaluation

The correlation between in silico and *in vivo* data reveals critical insights into the pharmacokinetics and distribution behavior of the various BEV formulations. The in silico predictions, generated using ADMET predictor software, provided an initial understanding of the absorption, distribution, metabolism, and excretion profiles across major organs, such as the liver, kidney, and brain, as well as plasma

Table I IC_{50} Values of BEV-API and BEV-API Containing NDDSs

Samples	IC_{50} (µg/mL)		
	Day 3- 48 h exposure	Day 7- 6 day exposure	Day 8- 48 h exposure
BEV-API	> 500	306.6 ± 22.6	> 500
BEV-PM	> 3500	> 3500	nd
AP-BEV + M1A-EXO	537.8 ± 15.2	292.9 ± 25.5	574.9 ± 46.9
BEV-CHI-NP	633.0 ± 23.0	336.4 ± 20.8	nd

BEV-API (500 µg/mL): 3355.7 nM; nd: Not determined

concentrations. These simulations indicated differential permeabilities and distribution patterns based on the molecular descriptors of each formulation, with variations particularly evident in diffusion coefficients and binding affinities [27].

When comparing these predictions with the *in vivo* pharmacokinetic data, a strong correlation was observed, particularly in the plasma concentration–time profiles and organ-specific distribution. The BEV-API formulation demonstrated rapid clearance and low tissue retention, as predicted by the in silico model (Fig. 4B). On the other hand, BEV-PM and BEV-CHI-NP showed prolonged circulation times and higher tissue uptake, consistent with the predicted higher stability and slower clearance rates. While the AP-BEV + M1A-EXO formulation demonstrated prolonged release and predicted higher binding affinities in silico, the *in vivo* PK and tumor concentration data (Fig. 8A) indicate that BEV-CHI particles achieved higher tumor accumulation. This discrepancy can be attributed to differences in the biodistribution and clearance mechanisms of the two formulations. The BEV-CHI particles benefit from the mucoadhesive properties of chitosan, which enhance retention at the tumor site, as well as its ability to interact with negatively charged tumor extracellular matrix components. In contrast, exosomes, despite their natural targeting ability and prolonged circulation, may experience higher uptake by the mononuclear phagocyte system (MPS), leading to a relatively reduced tumor accumulation. These findings highlight that while AP-BEV + M1A-EXO offers superior release control and systemic stability, BEV-CHI particles leverage their physicochemical properties to enhance tumor localization.

The data in Fig. 8B demonstrates a distinct variation in apoptotic cell percentages across the treated groups, with the AP-BEV + M1A-EXO group exhibiting the lowest percentage of apoptotic cells (11.23%).This observation suggests that the formulation might be providing a protective effect or might be less effective in inducing apoptosis compared to other treatments. In contrast, the Control (+) group, which represents untreated cancer cells, shows a high percentage of apoptosis (91.33%), possibly due to the progression of the disease or the physiological response of the cells in the absence of therapeutic intervention. The BEV-PM and BEV-CHI-NP formulations also show intermediate levels of apoptosis, with BEV-PM slightly outperforming BEV-CHI-NP, indicating that the polymeric micelle and chitosan-based nanoparticle formulations do induce cell death but perhaps not as efficiently as the AP-BEV + M1A-EXO formulation. The release profiles of AS1411 aptamer and M1A mRNA *in vivo* demonstrate distinct patterns in plasma and tumor tissues. AS1411 shows a rapid initial release in plasma, with concentrations peaking early at 1 h and subsequently declining over 48 h (Supplementary File-S4). In contrast, tumor accumulation of AS1411 steadily increases, reaching its maximum concentration around 48 h. This indicates efficient tumor localization and sustained retention, consistent with the targeting capabilities of the exosomal formulation [14].

For M1A, plasma concentrations start at moderate levels and gradually decrease over time, suggesting controlled systemic release. Tumor accumulation of M1A increases progressively and stabilizes after 8–12 h, maintaining elevated levels up to 48 h. This sustained release and tumor retention suggest that the formulation effectively protects and delivers the mRNA payload to the tumor microenvironment. Such release kinetics align with previous findings on nanoparticle-based delivery systems, where exosomes facilitate prolonged circulation and targeted delivery due to their biocompatibility and ability to escape rapid systemic clearance [18, 73].

Among the formulations, the AP-BEV + M1A-EXO demonstrated the highest tumor tissue partition coefficient (Kp) (4.74) and unbound tumor tissue partition coefficient (Kpuu) (4.74), with corresponding log10(Kp) and log10(Kpuu) values of 0.676, highlighting its superior tumor localization and retention. This enhanced accumulation aligns with the exosomal formulation's ability to efficiently deliver its payload through natural tumor-targeting mechanisms and prolonged systemic circulation [74]. BEV-CHI-NP showed moderately high tumor Kp (4.23) due to the mucoadhesive properties of chitosan, which enhance tissue retention, while BEV-PM exhibited slightly lower tumor Kp (3.92), suggesting limited penetration or retention compared to the other formulations.

Liver Kp values were notably higher for the AP-BEV + M1A-EXO (3.45) compared to BEV-CHI-NP (2.89) and BEV-PM (2.73), consistent with exosomes being preferentially taken up by the mononuclear phagocyte system (MPS) in the liver [75]. Kidney Kp values were lower across all formulations, with BEV-PM showing the lowest retention (Kp = 2.19), suggesting efficient systemic clearance pathways for this polymeric formulation. The spleen showed moderate Kp values across all formulations, indicative of MPS involvement in nanoparticle clearance. AP-BEV + M1A-EXO demonstrated slightly higher spleen Kp (2.68) compared to BEV-CHI-NP (2.41) and BEV-PM (2.26), consistent with exosome-mediated uptake Table II.

Protein and Transcript Analysis

The Western blot results in Fig. 8C reveal the expression levels of critical cancer biomarkers: CA 125, CA 19–9, CEA, and TYMS, with GAPDH serving as a housekeeping control. The AP-BEV + M1A-EXO group demonstrates notably lower levels of these biomarkers compared to other treatment groups and the Control (+) ($p < 0.05$). This suggests that the exosome-based formulation with M1A and AS1411, which targets specific molecular pathways, is highly effective in reducing the tumor's biomarker expression, possibly by interfering with tumor growth and metastasis-related pathways. The other formulations (BEV-PM and

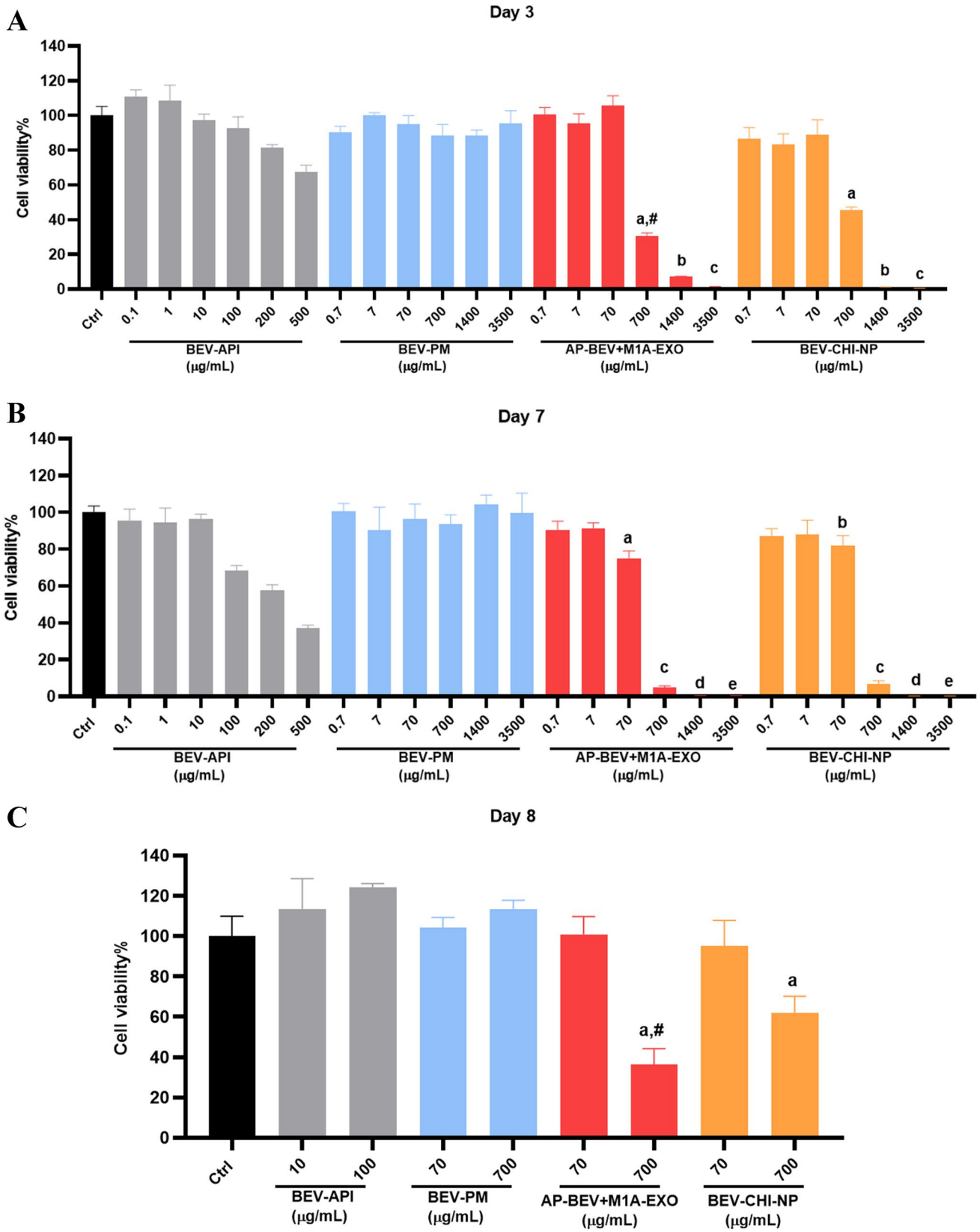
A
Day 3
Cell viability%
140
120
100
80
60
40
20
0
Ctrl
0.1
1
10
100
200
500
0.7
7
70
700
1400
3500
0.7
7
70
700
1400
3500
0.7
7
70
700
1400
3500
a,#
b
c
a
b
c
BEV-API (μg/mL)
BEV-PM (μg/mL)
AP-BEV+M1A-EXO (μg/mL)
BEV-CHI-NP (μg/mL)
B
Day 7
Cell viability%
a
c
d
e
b
c
d
e
C
Day 8
Cell viability%
10
100
70
700
70
700
70
700
a,#
a

◂**Fig. 6** **A** Cell viability of BEV-API and related drug delivery systems in HCTO for 48 h exposure.Statistical differences between BEV-API (100 µg/mL or 671.1 nM) vs. groups $^{a}p < 0.001$; BEV-API (200 µg/mL) vs. groups $^{b}p < 0.001$; BEV-API (500 µg/mL) vs. groups $^{c}p < 0.001$, and AP-BEV + M1A-EXO (700 µg/mL) vs. BEV-CHI-NP (700 µg/mL) $^{\#}p < 0.01$. Ctrl: Negative control group treated with human colon organoid culture medium. **B** Cell viability of BEV-API and NDDS in HCTO for 6-day exposure.Statistical differences between BEV-API (10 µg/mL) vs. groups $^{a}p < 0.05$; $^{b}p < 0.001$; BEV-API (100 µg/mL) vs. groups $^{c}p < 0.001$; BEV-API (200 µg/mL) vs. groups $^{d}p < 0.001$, and BEV-API (500 µg/mL) vs. groups $^{e}p < 0.001$. Ctrl: Negative control group treated with human colon organoid culture. **C** Cell viability of BEV-API and NDDS in established (day 8) HCTO for 48 h exposure. Statistical differences between BEV-API (100 µg/mL) vs. groups $^{a}p < 0.001$; and AP-BEV + M1A-EXO (700 µg/mL) vs. BEV-CHI-NP (700 µg/mL) $^{\#}p < 0.01$. Ctrl: The negative control group treated with human colon organoid culture medium

BEV-CHI-NP) also show reductions in biomarker levels but to a lesser extent, indicating their lower potency in biomarker suppression. Panels Fig. 8D and E further quantify the relative expression levels of CEA, CA19-9, and TYMS mRNA in the treated groups. The qRT-PCR results corroborate the Western blot findings, showing significantly reduced expression of these biomarkers in the AP-BEV + M1A-EXO group. The statistical significance indicated by asterisks (****$p < 0.0001$, **$p < 0.01$) underscores the efficacy of this formulation. The reduced expression levels in the AP-BEV + M1A-EXO group could be attributed to the targeted delivery of the BEV via exosomes, which allows for more precise interaction with tumor cells, effectively silencing gene expression. The minimal differences in biomarker expression between the Control (-) group (healthy mice) and treated groups (AP-BEV + M1A-EXO) indicate that this treatment could potentially normalize the aberrant expression levels seen in cancer, making it a promising candidate for reducing tumor burden without significant off-target effects.

The IHC staining in Fig. 8F provides a visual representation of the tumor and immune cell infiltration within the colorectal tissue. The AP-BEV + M1A-EXO and BEV-CHI-NP formulations demonstrate significantly reduced tumor cell infiltration, as evidenced by fewer red arrows compared to the Control (+) group. The reduction in tumor cell infiltration was ~ 65.4% for the AP-BEV + M1A-EXO formulation and 56.4% for the BEV-CHI-NP formulation. Furthermore, all tumor tissue measurements were validated using micro-CT scans to confirm the reduction in tumor volume in mm^3 (Supplementary File-S4,S5, and S6). This suggests that these formulations are effective in either directly reducing tumor cell viability or in enhancing immune cell-mediated tumor destruction [76, 77]. The yellow arrows denoting immune cell infiltration highlight the immune response's role in combating tumor cells, with the AP-BEV + M1A-EXO group possibly aiding in immune modulation due to the presence of exosomes, which are known to have immune-modulating properties. The healthier tissue architecture observed in the treated groups, especially in the AP-BEV + M1A-EXO, aligns with the reduced biomarker expression and increased apoptosis seen in the earlier panels. According to the Fig. 8G further elucidates the impact of the treatments on cell cycle progression. The AP-BEV + M1A-EXO formulation induces a shift towards G0/G1 phase arrest, which is associated with the suppression of cell proliferation. This shift is indicative of the formulation's ability to halt the cell cycle, thereby preventing the replication of cancerous cells. The other formulations (BEV-PM and BEV-CHI-NP) also show some degree of cell cycle arrest but are less pronounced than in the AP-BEV + M1A-EXO group. The Control (+) group exhibits a typical cancer cell cycle profile with fewer cells in G0/G1 and more in the S and G2/M phases, indicative of ongoing proliferation. The effectiveness of the AP-BEV + M1A-EXO formulation in inducing cell cycle arrest could be due to the synergistic effects of M1A and AS1411, which are known to target molecular pathways crucial for cell cycle regulation and apoptosis. The CA125-AF488 column reveals varying intensities of green fluorescence, reflecting differences in CA125 expression among the groups.

The merged images combine both signals, further highlighting the distribution of CA125 within the cells Fig. 8H. Notably, the BEV-PM group exhibits the highest intensity of CA125, indicating enhanced expression, followed by the negative control group. This is followed by BEV-CHI-NP and AP-BEV + M1A-EXO, which show moderate levels of CA125. The positive control shows a non-significant CA125 signal ($p > 0.05$), while the negative control exhibits maximal fluorescence ($p < 0.001$, ****). The bar graph quantifies fluorescence intensity (AU) for CA125-AF488 across the groups. Statistically significant differences are indicated, with the AP-BEV + M1A-EXO group showing the minimal expression after control (+) compared to other treatments. Statistical markers (e.g., *, **, ***) highlight significant differences between the groups, confirming the impact of the treatments on CA125 expression. The observed increase in CA125 levels following BEV treatment could be attributed to the tumor's adaptive response to VEGF inhibition. BEV targets VEGF, disrupting tumor angiogenesis and inducing hypoxic conditions within the tumor microenvironment. This hypoxia may stimulate the release of pro-inflammatory cytokines and tumor-associated glycoproteins like CA125 as part of a compensatory mechanism. Additionally, increased CA125 levels may reflect tumor cell stress or the immune system's response to treatment [78].

In summary, the AP-BEV + M1A-EXO formulation emerges as the most effective among the tested treatments, showing significant reductions in cancer biomarker expression, increased apoptosis, and pronounced cell cycle arrest. This formulation's superior performance can be attributed

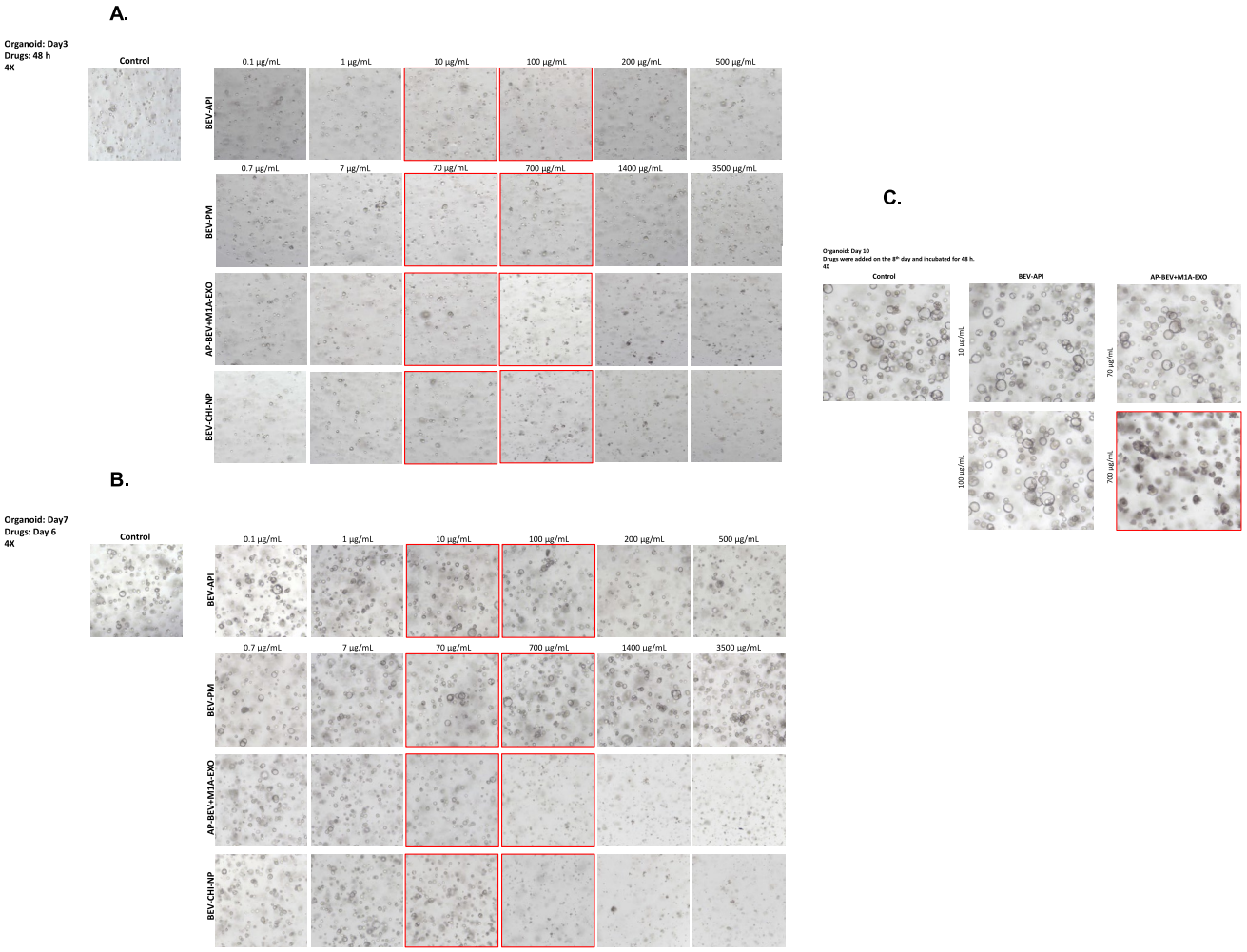

Fig. 7 Microscopic examination of HCTOs BEV-API and NDDS. **A** BEV-API and related drug delivery systems exposed to the day 3 HCTO for 48 h exposure; **B** BEV-API and related drug delivery systems exposed to the day 7 HCTO for 6-day exposure; **C** BEV-API and related drug delivery systems exposed to the day 8 HCTO for 48 h exposure. (Magnification rate 4X)

to the combined effects of targeted delivery via exosomes and the specific actions of M1A and AS1411, which likely enhance the precision and efficacy of BEV. The results highlight the potential of using advanced nanoparticle-based drug delivery systems for more effective colorectal cancer treatment, with minimal off-target effects, as evidenced by the closer resemblance of treated tissues to the healthy control.

Tissue-Level Visualization

Figure 7I illustrates cancerous areas within the intestinal tissue of mice, with a focus on comparing the effects of different therapeutic interventions. The control (-) shows significant brown staining, which is indicative of either non-specific binding or background activity, serving as a baseline for comparison with no targeted treatment. In contrast, the control (+) displays more discrete and consistent staining, confirming the successful expression of targeted proteins typically associated with the pathological state in untreated cancerous tissue. This validates the staining procedure and highlights the extent of protein presence in the untreated state.

In the AP-BEV + M1A-EXO treatment group, there is a marked reduction in staining intensity compared to the positive control. This suggests that the combination of BEV-conjugated, M1A and aptamer-loaded exosomes has effectively modulated or suppressed the protein expression linked to tumor progression [18]. The reduction in staining might reflect the downregulation of specific cancer-related

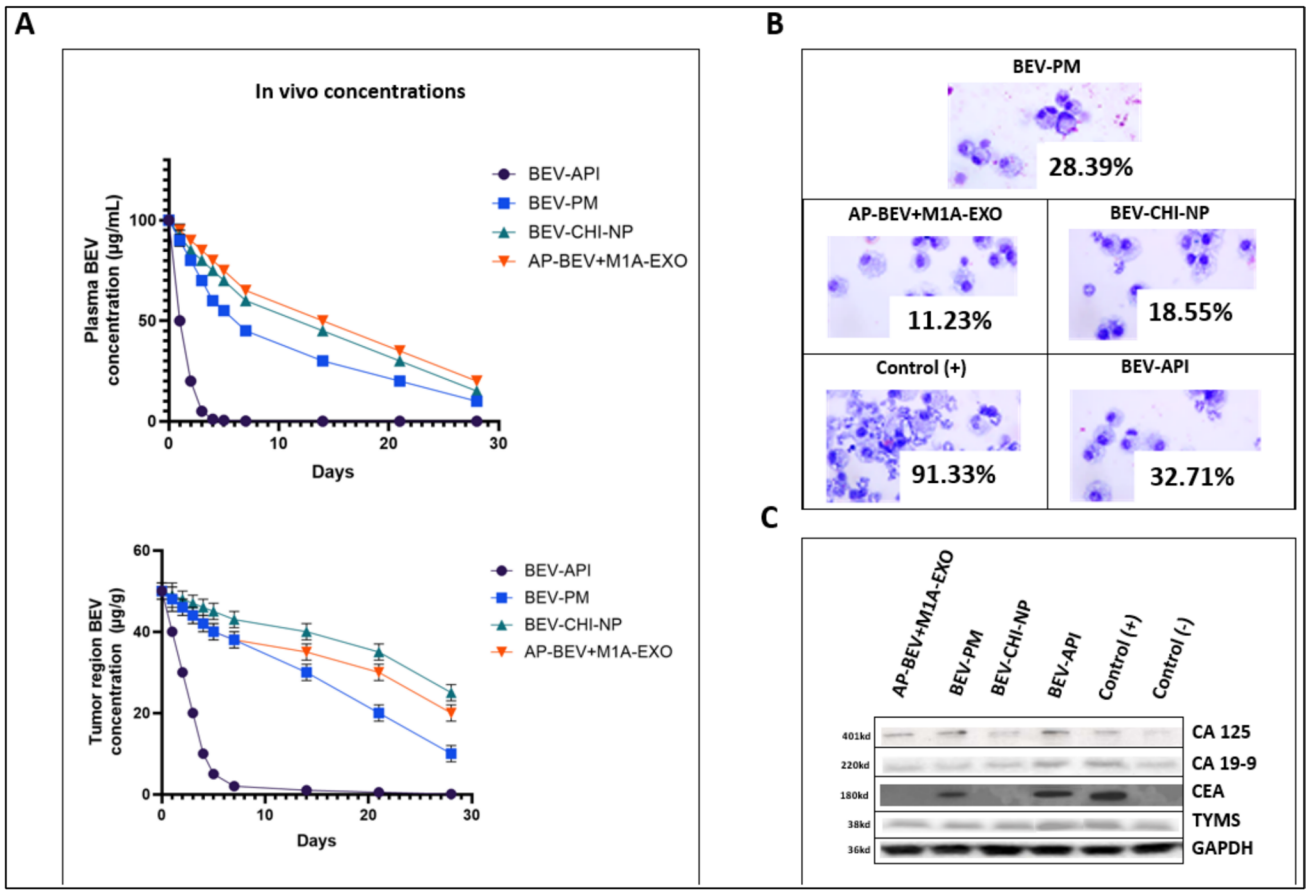

Fig. 8 *In vivo* efficacy of various BEV Formulations in colorectal cancer model **A** *In vivo* concentration of BEV over time in plasma and tumor region, it displays the concentration–time curves for different BEV formulations (BEV-API, BEV-PM, BEV-CHI-NP, AP-BEV + M1A-EXO) in plasma and tumor regions across 28 days. **B** Apoptotic cell detection in colorectal cancer tissue after 28 days of treatment **C** Western analysis of colorectal cancer biomarkers (CA 125, CA 19–9, CEA, and TYMS) **D** Quantitative rt-PCR analysis of CEA and CA19-9 mRNA expression **E** Quantitative rt-PCR analysis of housekeeping gene, CA125 and TYMS mRNA expression **F** IHC staining depicting the presence of tumor cells and immune cell infiltration in colorectal cancer tissues treated with different formulations compared to control groups **G**) Flow cytometry analysis of cell cycle distribution in colorectal cancer cells **H** Fluorescence microscope images using DAPI filter and AF488-stained cells CA125 Expression after treatment with formulations I) Comparative histological evaluation of the tissues after treatment

proteins or disruption of pathways crucial to tumor growth. The BEV-PM treatment group presents moderate brown staining, showing that this formulation exerts a therapeutic effect by targeting and reducing protein expression in the cancerous area, though not as pronounced as the exosome-based delivery system [47]. The more uniform distribution of staining could suggest broader yet less intense activity within the tissue, likely due to slower or more gradual drug release from the polymer matrix.

The most concentrated staining is observed in the BEV-CHI-NP group, where localized clusters of brown staining suggest enhanced drug delivery and retention at specific tumor sites. The chitosan nanoparticles may be facilitating more precise delivery of BEV, possibly improving cellular uptake and interaction with cancer cells [72]. This increased targeting could reflect a more robust anti-tumor response, as nanoparticles are known to enhance permeability and retention in tumor tissue, leading to greater accumulation and activity of the therapeutic agent. In a nutshell, these findings demonstrate the varying efficacy of different delivery systems in modulating protein expression within cancerous tissue. The nanoparticle-based and exosome-based therapies show potential for more precise targeting and enhanced therapeutic outcomes compared to polymer matrix-based delivery, emphasizing the importance of drug delivery method in cancer treatment strategies.

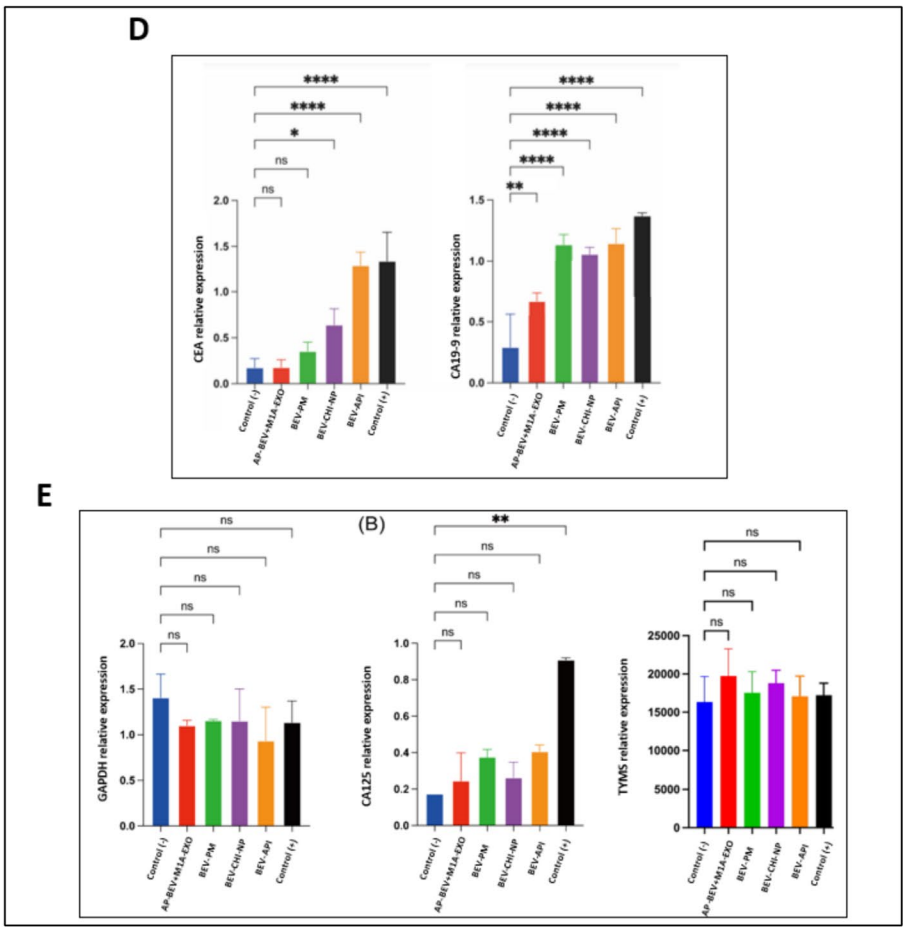

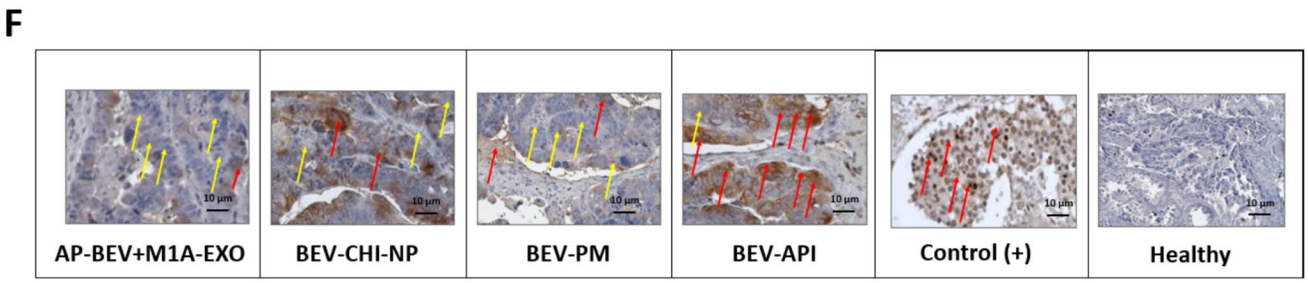

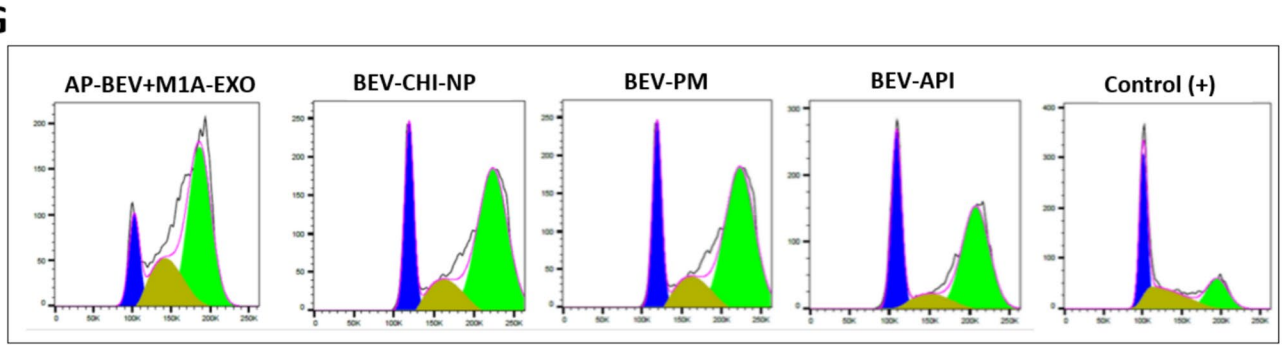

Fig. 8 (continued)

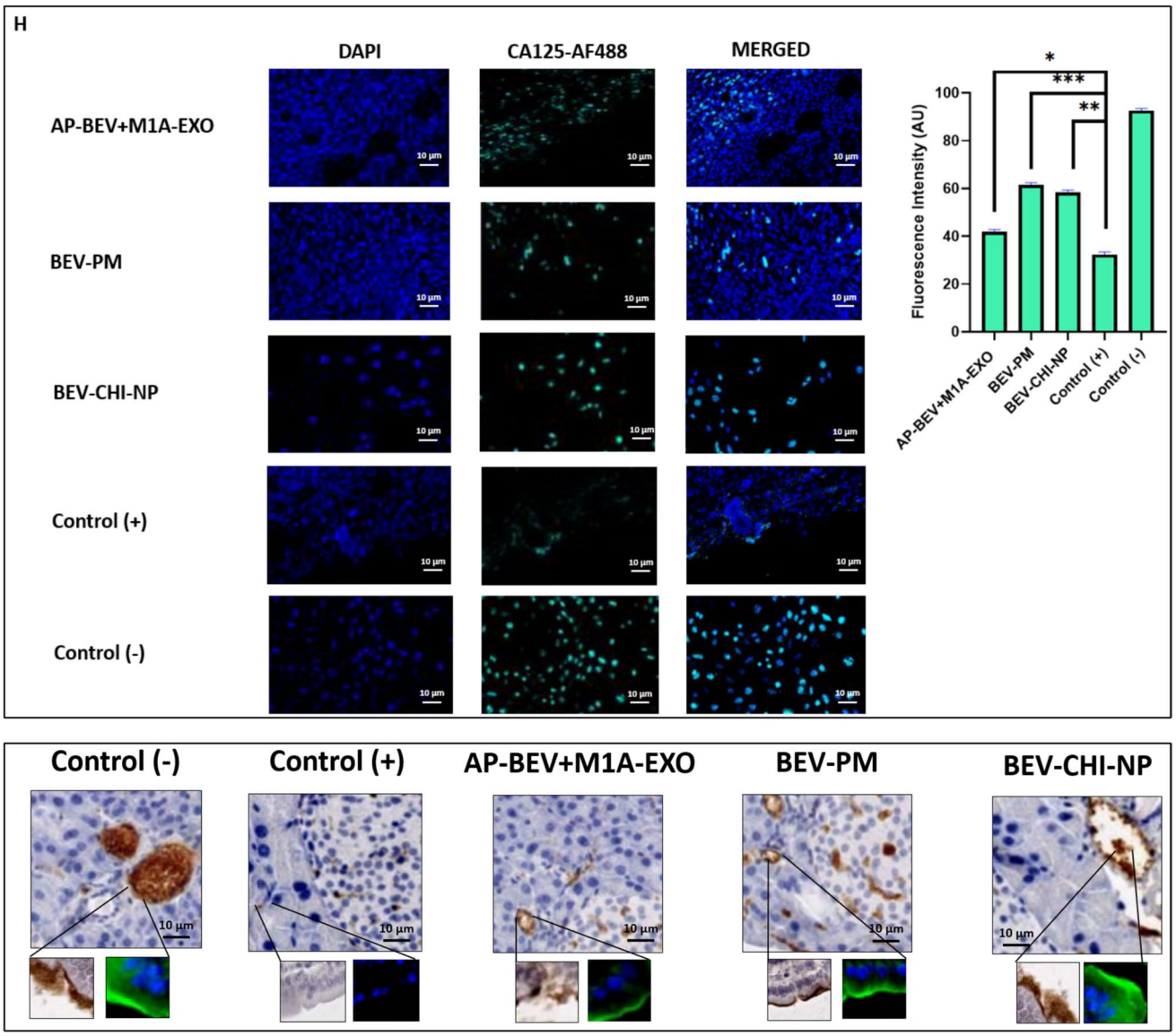

Fig. 8 (continued)

Conclusion

The results of this study underscore the significant potential of aptamer- and exosome-based nanoparticle formulations in targeted colorectal cancer treatment. Notably, the AP-BEV + M1A-EXO formulation exhibited a four-fold improvement in therapeutic efficacy compared to traditional BEV-based therapies, as evidenced by a substantial reduction in tumor volume (65.4%) and a decrease in tumor biomarker levels by more than 50%, in parallel with the results obtained with HCTO in vitro. This dual targeting approach, combining the specificity of AS1411 with the delivery precision of exosomes, offers a promising strategy for increasing the therapeutic index of anti-cancer agents. These findings provide a compelling case for the further development and clinical application of these innovative drug delivery platforms, with the potential to revolutionize the management of colorectal cancer and other solid tumors.

Table II Tissue Partition Coefficient (K_p) and Unbound tissue Partition Coefficient (K_{puu}) for Formulations

BEV-CHI-NP						
Tissue	C_{tissue} (µg/g)	C_{plasma} (µg/mL)	K_p	$\log_{10}(K_p)$	K_{puu}	$\log_{10}(K_{puu})$
Liver	14.75	5.10	2.89	0.461	2.89	0.461
Kidney	11.40	5.10	2.24	0.350	2.24	0.350
Tumor	21.55	5.10	4.23	0.627	4.23	0.627
Spleen	12.30	5.10	2.41	0.382	2.41	0.382
BEV-PM						
Tissue	**C_{tissue} (µg/g)**	**C_{plasma} (µg/mL)**	**K_p**	**$\log_{10}(K_p)$**	**K_{puu}**	**$\log_{10}(K_{puu})$**
Liver	13.5	4.95	2.73	0.436	2.73	0.436
Kidney	10.85	4.95	2.19	0.34	2.19	0.34
Tumor	19.4	4.95	3.92	0.594	3.92	0.594
Spleen	11.2	4.95	2.26	0.354	2.26	0.354
AP-BEV + M1A-EXO						
Tissue	**C_{tissue} (µg/g)**	**C_{plasma} (µg/mL)**	**K_p**	**$\log_{10}(K_p)$**	**K_{puu}**	**$\log_{10}(K_{puu})$**
Liver	18.3	5.3	3.45	0.538	3.45	0.538
Kidney	12.95	5.3	2.44	0.387	2.44	0.387
Tumor	25.1	5.3	4.74	0.676	4.74	0.676
Spleen	14.2	5.3	2.68	0.428	2.68	0.428

Supplementary Information The online version contains supplementary material available at https://doi.org/10.1208/s12249-025-03069-9.

Acknowledgements We would like to thank Semir Beyaz and Onur Eskiocak for their guidance on the protocols for organoid generation.

Author Contribution B.Uner: Conceptualization, Writing – original draft, Writing – review & editing, Methodology, Investigation, Formal analysis, Data curation, Validation, Supervision. E.O. Akyildiz: Methodology, Investigation, Writing – original draft, Rewiev & editing, Formal analysis, Data curation. K. Kolci: Writing – original draft, Writing – review & editing, Formal analysis, Data curation. R. Reis: Writing – review & editing, Writing – original draft, Validation, Supervision, Methodology, Formal analysis, Data curation.

Data Availability The data that support the findings of this study can be obtained from the corresponding author upon reasonable request.

Declarations

Conflict of Interest The authors declare that there are no conflicts of interest related to this work.

References

1. Mianowska M, Zaremba-Czogalla M, Zygmunt A, Mahmud M, Süss R, Gubernator J. Dual Role of Vitamin C-Encapsulated Liposomal Berberine in Effective Colon Anticancer Immunotherapy. Pharmaceuticals. 2024;17(1):5.
2. Kesharwani P, Ma R, Sang L, et al. (2023) Gold nanoparticles and gold nanorods in the landscape of cancer therapy. Mol Cancer. 2023;22(1):98. https://doi.org/10.1186/s12943-023-01798-8.
3. De Leo V, Milano F, Mancini E, et al. Encapsulation of Curcumin-Loaded Liposomes for Colonic Drug Delivery in a pH-Responsive Polymer Cluster Using a pH-Driven and Organic Solvent-Free Process. Molecules. 2018;23(4). https://doi.org/10.3390/molecules23040739
4. Cevik O, Acidereli H, Turut FA, Yildirim S, Acilan C. Cabazitaxel exhibits more favorable molecular changes compared to other taxanes in androgen-independent prostate cancer cells. J Biochem Mol Toxicol. 2020;34(9): e22542. https://doi.org/10.1002/jbt.22542.
5. Burr AH, Ji J, Ozler K, et al. Excess Dietary Sugar Alters Colonocyte Metabolism and Impairs the Proliferative Response to Damage. Cell Mol Gastroenterol Hepatol. 2023;16(2):287–316.
6. Fei Y, Wang Y, Pang Y, et al. Xylooligosaccharide Modulates Gut Microbiota and Alleviates Colonic Inflammation Caused by High Fat Diet Induced Obesity. Original Research Front Physiol. 2020;2020:10. https://doi.org/10.3389/fphys.2019.01601.
7. Zhang L, Yao L, Zhao F, et al. Protein and Peptide-Based Nanotechnology for Enhancing Stability, Bioactivity, and Delivery of Anthocyanins. Adv Healthcare Mater. 2023;12(25):2300473. https://doi.org/10.1002/adhm.202300473.
8. Fabozzi A, Della Sala F, di Gennaro M, et al. Design of functional nanoparticles by microfluidic platforms as advanced drug delivery systems for cancer therapy. Lab on a Chip. 2023;23(5):1389–409. https://doi.org/10.1039/D2LC00933A.
9. Zhang J, Wang S, Zhang D, et al. Nanoparticle-based drug delivery systems to enhance cancer immunotherapy in solid tumors. Review Front Immunol. 2023;2023:14. https://doi.org/10.3389/fimmu.2023.1230893.
10. Chen ER, Kaiser PK. Therapeutic Potential of the Ranibizumab Port Delivery System in the Treatment of AMD: Evidence to Date. Clin Ophthalmol. 2020;14:1349–55. https://doi.org/10.2147/opth.S194234.
11. Del Amo EM, Rimpelä AK, Heikkinen E, et al. Pharmacokinetic aspects of retinal drug delivery. Prog Retin Eye Res. 2017;57:134–85. https://doi.org/10.1016/j.preteyeres.2016.12.001.
12. Hilberg F, Roth GJ, Krssak M, et al. BIBF 1120: triple angiokinase inhibitor with sustained receptor blockade and good antitumor efficacy. Cancer Res. 2008;68(12):4774–82. https://doi.org/10.1158/0008-5472.Can-07-6307.
13. Mirabelli P, Peebo BB, Xeroudaki M, Koulikovska M, Lagali N. Early effects of dexamethasone and anti-VEGF therapy in an inflammatory corneal neovascularization model. Exp Eye Res. 2014;125:118–27.

14. Van den Avont A, Sharma-Walia N. Anti-nucleolin aptamer AS1411: an advancing therapeutic. Front Mol Biosci. 2023;10:1217769.
15. Iman M, Moosavian SA, Zamani P, Jaafari MR. Preparation of AS1411 aptamer-modified PEGylated liposomal doxorubicin and evaluation of its anti-cancer effects in vitro and in vivo. J Drug Deliv Sci Technol. 2023;81: 104255.
16. Liu Y, Zhang S, Gao X, Ru Y, Gu X, Hu X. Research progress of N1-methyladenosine RNA modification in cancer. Cell Commun Signal. 2024;22(1):79.
17. Xue M, Mi S, Zhang Z, et al. MFAP2, upregulated by m1A methylation, promotes colorectal cancer invasiveness via CLK3. Cancer Med. 2023;12(7):8403–14.
18. Jiang C, Tian Y, Xu C, Zhang H, Gu L. Landscape of N1-methyladenosin (m1A) modification pattern in colorectal cancer. Cancer Reports. 2024;7(2): e1965.
19. Alami-Milani M, Zakeri-Milani P, Valizadeh H, Salehi R, Jelvehgari M. Preparation and evaluation of PCL-PEG-PCL micelles as potential nanocarriers for ocular delivery of dexamethasone. Iran J Basic Med Sci. 2018;21(2):153–164. https://doi.org/10.22038/ijbms.2017.26590.6513
20 Atassi Y, Said M, Tally M, Kouba L. Synthesis and characterization of chitosan-g-poly(AMPS-co-AA-co-AM)/ground basalt composite hydrogel: antibacterial activity. Polym Bull. 2020;77(10):5281–302. https://doi.org/10.1007/s00289-019-03017-1.
21. Kiplagat A, Martin DR, Onani MO, Meyer M. Aptamer-conjugated magnetic nanoparticles for the efficient capture of cancer biomarker proteins. J Magn Magn Mater. 2020;497: 166063.
22. Pham CV, Chowdhury R, Patel S, et al. An aptamer-guided fluorescence polarisation platform for extracellular vesicle liquid biopsy. J Extracellular Vesicles. 2024;13(9): e12502. https://doi.org/10.1002/jev2.12502.
23 Iwamoto N, Umino Y, Aoki C, Yamane N, Hamada A, Shimada T. Fully validated LCMS bioanalysis of Bevacizumab in human plasma using nano-surface and molecular-orientation limited (nSMOL) proteolysis. Drug Metab Pharmacokinet. 2016;31(1):46–50. https://doi.org/10.1016/j.dmpk.2015.11.004.
24. M10 Ig. Bioanalytical Method Validation Guidance for Industry. In: Use CfMPfH, editor. 2022.
25. ich. validation of analytical procedures:text and methodology. In: Harmonisation Ico, editor. 2005.
26. Min Jung J, Lip Jung Y, Han Kim S, Sung Lee D, Thambi T. Injectable hydrogel imbibed with camptothecin-loaded mesoporous silica nanoparticles as an implantable sustained delivery depot for cancer therapy. J Coll Interface Sci. 2023;636:328–40. https://doi.org/10.1016/j.jcis.2023.01.028.
27 Kingsbury JS, Saini A, Auclair SM, et al. A single molecular descriptor to predict solution behavior of therapeutic antibodies. Sci Adv. 2020;6(32):eabb0372. https://doi.org/10.1126/sciadv.abb0372.
28. Ishiguro S, Robben N, Burghart R, et al. Cell Wall Membrane Fraction of Chlorella sorokiniana Enhances Host Antitumor Immunity and Inhibits Colon Carcinoma Growth in Mice. Integr Cancer Ther Jan-Dec. 2020;19:1534735419900555. https://doi.org/10.1177/1534735419900555.
29. Dmitrieva-Posocco O, Wong AC, Lundgren P, et al. β-Hydroxybutyrate suppresses colorectal cancer. Nature. 2022;605(7908):160–5. https://doi.org/10.1038/s41586-022-04649-6.
30. Luis de Redín I, Expósito F, Agüeros M, et al. In vivo efficacy of bevacizumab-loaded albumin nanoparticles in the treatment of colorectal cancer. Drug Deliv Transl Res. 2020;10(3):635–645. https://doi.org/10.1007/s13346-020-00722-7
31. Clift CL, Mehta A, Drake RR, Angel PM. Multiplexed imaging mass spectrometry of histological staining, N-glycan and extracellular matrix from one tissue section: a tool for fibrosis research. Multiplexed Imaging: Methods Protocol. 2021:313–329.
32. Elumalai K, Srinivasan S, Shanmugam A. Review of the efficacy of nanoparticle-based drug delivery systems for cancer treatment. Biomed Technol. 2024;5:109–22. https://doi.org/10.1016/j.bmt.2023.09.001.
33. Ezike TC, Okpala US, Onoja UL, et al. Advances in drug delivery systems, challenges and future directions. Heliyon. 2023;9(6): e17488. https://doi.org/10.1016/j.heliyon.2023.e17488.
34 Ul-Islam M, Alabbosh KF, Manan S, Khan S, Ahmad F, Ullah MW. Chitosan-based nanostructured biomaterials: Synthesis, properties, and biomedical applications. Adv Ind Eng Polym Res. 2024;7(1):79–99. https://doi.org/10.1016/j.aiepr.2023.07.002.
35. Kimoto M, Shermane Lim YW, Hirao I. Molecular affinity rulers: systematic evaluation of DNA aptamers for their applicabilities in ELISA. Nucleic Acids Res. 2019;47(16):8362–74. https://doi.org/10.1093/nar/gkz688.
36. Piccolo KA, McNeil B, Crouse J, et al. Ligand specificity and affinity in the sulforhodamine B binding RNA aptamer. Biochem Biophys Res Commun. 2020;529(3):666–71. https://doi.org/10.1016/j.bbrc.2020.06.056.
37. Yang R, Tang S, Xie X, et al. Enhanced Ocular Delivery of Beva via Ultra-Small Polymeric Micelles for Noninvasive Anti-VEGF Therapy. Adv Mater. 2024:2314126. https://doi.org/10.1002/adma.202314126.
38. Guastaferro M, Baldino L, Cardea S, Reverchon E. Supercritical processing of PCL and PCL-PEG blends to produce improved PCL-based porous scaffolds. J Supercrit Fluids. 2022;186: 105611.
39. Ravikumar R, Ganesh M, Senthil V, Ramesh YV, Jakki SL, Choi EY. Tetrahydro curcumin loaded PCL-PEG electrospun transdermal nanofiber patch: Preparation, characterization, and in vitro diffusion evaluations. J Drug Deliv Sci Technol. 2018;44:342–8. https://doi.org/10.1016/j.jddst.2018.01.016.
40. Qiao C, Ma X, Wang X, Liu L. Structure and properties of chitosan films: Effect of the type of solvent acid. Lwt. 2021;135: 109984.
41. Ren L, Zeng F, Deng J, et al. Inflammatory osteoclasts-derived exosomes promote bone formation by selectively transferring lncRNA LIOCE into osteoblasts to interact with and stabilize Osterix. FASEB J. 2022;36(2): e22115.
42. Ma S, Wu J, Hu H, et al. Novel fusion peptides deliver exosomes to modify injectable thermo-sensitive hydrogels for bone regeneration. Materials Today Bio. 2022;13: 100195.
43. Goetzl EJ, Srihari VH, Guloksuz S, Ferrara M, Tek C, Heninger GR. Neural cell-derived plasma exosome protein abnormalities implicate mitochondrial impairment in first episodes of psychosis. FASEB J. 2021;35(2): e21339.
44. Sulthana S, Aryal S. Tumor-derived extracellular vesicles hybridized liposomes in cancer therapy. Biophys J. 2023;122(3):455a–6a.
45. Hammad RW, Sanad RA-B, Abdelmalak NS, Latif R. Architecting novel multilayer nanosponges for co-administration of two drugs managing high-risk type II diabetes mellitus patients suffering from cardiovascular diseases. Int J Biol Macromolecules. 2022;220:1429–1443. https://doi.org/10.1016/j.ijbiomac.2022.09.099
46. Kalam MA, Iqbal M, Alshememry A, Alkholief M, Alshamsan A. Development and Evaluation of Chitosan Nanoparticles for Ocular Delivery of Tedizolid Phosphate. Molecules. 2022;27(7). https://doi.org/10.3390/molecules27072326.
47 Zheng Y, Li M, Weng B, Mao H, Zhao J. Exosome-based delivery nanoplatforms: next-generation theranostic platforms for breast cancer. Biomater Sci. 2022;10(7):1607–25. https://doi.org/10.1039/D2BM00062H.

48. Wu KY, Joly-Chevrier M, Akbar D, Tran SD. Overcoming Treatment Challenges in Posterior Segment Diseases with Biodegradable Nano-Based Drug Delivery Systems. Pharmaceutics. 2023;15(4). https://doi.org/10.3390/pharmaceutics15041094.
49. Barnes CP, Sell SA, Boland ED, Simpson DG, Bowlin GL. Nanofiber technology: Designing the next generation of tissue engineering scaffolds. Adv Drug Deliv Rev. 2007;59(14):1413–1433. https://doi.org/10.1016/j.addr.2007.04.022.
50. Gao J, Li A, Hu J, Feng L, Liu L, Shen Z. Recent developments in isolating methods for exosomes. Front Bioeng Biotechnol. 2022;10:1100892. https://doi.org/10.3389/fbioe.2022.1100892.
51. Yamaguchi S, Ito S, Masuda T, Couraud P-O, Ohtsuki S. Novel cyclic peptides facilitating transcellular blood-brain barrier transport of macromolecules in vitro and in vivo. J Control Release. 2020;321:744–55. https://doi.org/10.1016/j.jconrel.2020.03.001.
52. Valadi H, Ekström K, Bossios A, Sjöstrand M, Lee JJ, Lötvall JO. Exosome-mediated transfer of mRNAs and microRNAs is a novel mechanism of genetic exchange between cells. Nat Cell Biol. 2007;9(6):654–659. https://doi.org/10.1038/ncb1596.
53. Desai N, Rana D, Salave S, et al. Chitosan: A Potential Biopolymer in Drug Delivery and Biomedical Applications. Pharmaceutics. 2023;15(4). https://doi.org/10.3390/pharmaceutics15041313.
54. Stiepel RT, Pena ES, Ehrenzeller SA, et al. A predictive mechanistic model of drug release from surface eroding polymeric nanoparticles. J Control Release. 2022;351:883–895. https://doi.org/10.1016/j.jconrel.2022.09.067.
55. Beach MA, Nayanathara U, Gao Y, et al. Polymeric Nanoparticles for Drug Delivery. Chem Rev. 2024;124(9):5505–5616. https://doi.org/10.1021/acs.chemrev.3c00705.
56. Kar R, Dhar R, Mukherjee S, et al. Exosome-Based Smart Drug Delivery Tool for Cancer Theranostics. ACS Biomater Sci Eng. 2023;9(2):577–594. https://doi.org/10.1021/acsbiomaterials.2c01329.
57. Wang W, Sun H, Duan H, et al. Isolation and usage of exosomes in central nervous system diseases. CNS Neurosci Ther. 2024;30(3):e14677. https://doi.org/10.1111/cns.14677.
58. Sun K, Zheng X, Jin H, Yu F, Zhao W. Exosomes as CNS Drug Delivery Tools and Their Applications. Pharmaceutics. 2022;14(10) https://doi.org/10.3390/pharmaceutics14102252.
59. Zhang X, Zhang M, Cui H, et al. Autophagy-modulating biomembrane nanostructures: A robust anticancer weapon by modulating the inner and outer cancer environment. J Control Release. 2024;366:85–103.
60. Wang J, Zhu M, Nie G. Biomembrane-based nanostructures for cancer targeting and therapy: from synthetic liposomes to natural biomembranes and membrane-vesicles. Adv Drug Deliv Rev. 2021;178: 113974.
61. Garriga R, Herrero-Continente T, Palos M, et al. Toxicity of Carbon Nanomaterials and Their Potential Application as Drug Delivery Systems: In Vitro Studies in Caco-2 and MCF-7 Cell Lines. Nanomaterials. 2020;10(8):1617. https://doi.org/10.3390/nano10081617.
62. dos Santos AM, Carvalho SG, Ferreira LMB, Chorilli M, Gremião MPD. Understanding the role of electrostatic interactions on the association of 5-fluorouracil to chitosan-TPP nanoparticles. Colloids Surf, A. 2022;640: 128417.
63. Ahmed H, Bergmann F, Zeitlinger M. Protein Binding in Translational Antimicrobial Development-Focus on Interspecies Differences. Antibiotics (Basel). 2022;11(7) https://doi.org/10.3390/antibiotics11070923.
64. Herrera C, Harman S, Aldon Y, et al. The entry inhibitor DS003 (BMS-599793): a BMS-806 analogue, provides superior activity as a pre-exposure prophylaxis candidate. AIDS. 2021;35(12):1907–17. https://doi.org/10.1097/qad.0000000000002974.
65. Lau NCH, Yam JWP. From Exosome Biogenesis to Absorption: Key Takeaways for Cancer Research. Cancers (Basel). 2023;15(7). https://doi.org/10.3390/cancers15071992.
66 Ferreira D, Moreira JN, Rodrigues LR. New advances in exosome-based targeted drug delivery systems. Crit Rev Oncol/Hematol. 2022;172:103628. https://doi.org/10.1016/j.critrevonc.2022.103628.
67. Zhang Y, Bi J, Huang J, Tang Y, Du S, Li P. Exosome: a review of its classification, isolation techniques, storage, diagnostic and targeted therapy applications. Int J Nanomedicine. 2020:6917–6934. https://doi.org/10.2147/IJN.S264498.
68. Hatmal MM, Alshaer W, Al-Hatamleh MAI, et al. Comprehensive Structural and Molecular Comparison of Spike Proteins of SARS-CoV-2, SARS-CoV and MERS-CoV, and Their Interactions with ACE2. Cells. 2020;9(12). https://doi.org/10.3390/cells9122638.
69. Xu S, Yuan H, Li L, Yang K, Zhao L. Computational screening of potential bromodomain-containing protein 2 inhibitors for blocking SARS-CoV-2 infection through pharmacophore modeling, molecular docking and molecular dynamics simulation. Arab J Chem. 2024;17(1):105365. https://doi.org/10.1016/j.arabjc.2023.105365.
70. Bie L, Wang Y, Jiang F, Xiao Z, Zhang L, Wang J. Insights into the binding mode of AS1411 aptamer to nucleolin. Front Mol Biosci. 2022;9:1025313. https://doi.org/10.3389/fmolb.2022.1025313.
71. Sonin D, Pochkaeva E, Zhuravskii S, et al. Biological safety and biodistribution of chitosan nanoparticles. Nanomaterials. 2020;10(4):810.
72. Yee Kuen C, Masarudin MJ. Chitosan nanoparticle-based system: A new insight into the promising controlled release system for lung cancer treatment. Molecules. 2022;27(2):473.
73. Broudic K, Amberg A, Schaefer M, Spirkl HP, Bernard MC, Desert P. Nonclinical safety evaluation of a novel ionizable lipid for mRNA delivery. Toxicol Appl Pharmacol. 2022;451:116143. https://doi.org/10.1016/j.taap.2022.116143.
74. Trünkle C, Lechner C, Korr D, et al. Concentration Dependence of the Unbound Partition Coefficient Kp(uu) and Its Application to Correct for Exposure-Related Discrepancies between Biochemical and Cellular Potency of KAT6A Inhibitors. Drug Metab Dispos. 2020;48(7):553–62. https://doi.org/10.1124/dmd.120.090563.
75. Wan Z, Zhao L, Lu F, et al. Mononuclear phagocyte system blockade improves therapeutic exosome delivery to the myocardium. Theranostics. 2020;10(1):218–30. https://doi.org/10.7150/thno.38198.
76 Fan D, Cao Y, Cao M, Wang Y, Cao Y, Gong T. Nanomedicine in cancer therapy. Sig Transduct Target Ther. 2023;8(1):293. https://doi.org/10.1038/s41392-023-01536-y.
77. Cui S, Liu H, Cui G. Nanoparticles as drug delivery systems in the treatment of oral squamous cell carcinoma: current status and recent progression. Rev Front Pharmacol. 2023;14. https://doi.org/10.3389/fphar.2023.1176422.
78. Reardon DA, Freeman G, Wu C, et al. Immunotherapy advances for glioblastoma. Neuro Oncol. 2014;16(11):1441–58. https://doi.org/10.1093/neuonc/nou212.

Authors and Affiliations

Burcu Uner[1] · Erdogan Oguzhan Akyildiz[2,3] · Kubra Kolci[4,5] · Onur Eskiocak[2] · Rengin Reis[4] · Semir Beyaz[2]

✉ Burcu Uner
uner.burcu@yahoo.com

1 Department of Pharmaceutical and Administrative Sciences, University of Health Science and Pharmacy in St. Louis, St. Louis, Missouri 63110, USA

2 Cold Spring Harbor Laboratory, Cold Spring Harbor, New York 11724, USA

3 Department of Molecular Biology and Genetics, Faculty of Engineering and Natural Sciences, Acibadem Mehmet Ali Aydinlar University, Istanbul 34755, Turkey

4 Department of Pharmaceutical Toxicology, Faculty of Pharmacy, Acibadem Mehmet Ali Aydinlar University, Istanbul 34755, Turkey

5 Department of Pharmaceutical Toxicology, Faculty of Pharmacy, Yeditepe University, Istanbul 34755, Turkey